

# 1 Ventilation and low pollution enhancing new particle formation in 2 Milan, Italy

3 Myriam Agrò<sup>1</sup>, Manuel Bettineschi<sup>1</sup>, Silvia Melina<sup>2,a</sup>, Diego Aliaga<sup>1,b,c</sup>, Andrea Bergomi<sup>2</sup>, Beatrice Biffi<sup>3</sup>,  
4 Alessandro Bigi<sup>4</sup>, Giancarlo Ciarelli<sup>1</sup>, Cristina Colombi<sup>3</sup>, Paola Fermo<sup>2</sup>, Ivan Grigioni<sup>2</sup>, Veli-Matti  
5 Kerminen<sup>1</sup>, Markku Kulmala<sup>1</sup>, Janne Lampilahti<sup>1</sup>, Angela Marinoni<sup>5</sup>, Celestine Oliewo<sup>4,6</sup>, Juha Sulo<sup>1,d</sup>,  
6 Gianluigi Valli<sup>7</sup>, Roberta Vecchi<sup>7</sup>, Tuukka Petäjä<sup>1</sup>, Katrianne Lehtipalo<sup>1,8</sup>, Federico Bianchi<sup>1</sup>

7 <sup>1</sup>Institute for Atmospheric and Earth System Research / Physics, Faculty of Science, University of Helsinki, [00014](#), Helsinki,  
8 [00014](#), Finland

9 <sup>2</sup>Department of Chemistry, University of Milan, 20133, Milan, Italy

10 <sup>3</sup>Air Quality Department, Regional Agency for Environmental Protection of Lombardy, [20124](#), Milan, [20124](#), Italy

11 <sup>4</sup>Department of Engineering, University of Modena and Reggio Emilia, [41125](#), Modena, [41125](#), Italy

12 <sup>5</sup>Institute of Atmospheric Sciences and Climate, National Research Council of Italy, [40129](#), Bologna, [40129](#), Italy

13 <sup>6</sup>Scuola Universitaria Superiore IUSS, 27100, Pavia, Italy

14 <sup>7</sup>Department of Physics, University of Milan, 20133, Milan, Italy

15 <sup>8</sup>Atmospheric Composition Research, Finnish Meteorological Institute, [00101](#), Helsinki, [00101](#), Finland

16 <sup>a</sup>now at: Ecogeo s.r.l., 24122, Bergamo, Italy

17 <sup>b</sup>now at: Department of Environmental Science, Stockholm University, [141810691](#), Stockholm, Sweden

18 <sup>c</sup>now at: Bolin Centre for Climate Research, Stockholm University, [141810691](#), Stockholm, Sweden

19 <sup>d</sup>now at: School of Earth and Atmospheric Sciences, Queensland University of Technology, [4001](#), Brisbane, [4067](#), Australia

20 *Correspondence to:* Myriam Agrò ([myriam.agro@helsinki.fi](mailto:myriam.agro@helsinki.fi)) [and Federico Bianchi \(\[federico.bianchi@helsinki.fi\]\(mailto:federico.bianchi@helsinki.fi\)\)](#)

21 **Abstract.** New pParticle fFormation (NPF) is a crucial process that significantly affects the number of atmospheric particles,  
22 forming a substantial portion of the total aerosol population. Therefore, it has important implications for both human health  
23 and climate. While extensive research has been conducted in rural areas of the Po Valley, Italy, there is a substantial lack of  
24 continuous measurements with state-of-the-art instruments in Milan, one of the most industrialized and densely populated  
25 cities in the region. This study aims to address this gap by analysing one year of detailed particle number size distribution  
26 measurements between 1.2 and 480 nm at an urban background site in Milan. These data were used to examine the occurrence  
27 and characteristics of NPF and to identify how the meteorological and air pollution conditions affect it. We show that a cleaner  
28 atmosphere, meaning lower concentrations of air pollutants and lower condensation sink, and a higher ventilation promote  
29 NPF. Detailed modelling of the air masses history further revealed that a longer residence time in the Po Valley and a greater  
30 exposure to anthropogenic emissions ~~sources~~ inhibit NPF. Furthermore, we show that strong winds, particularly from the  
31 northwest sector (e.g., Foehn winds), facilitate NPF, likely by reducing the condensation sink for precursor vapours. This  
32 locates Milan among the urban sites where atmospheric cleaning enhances NPF, providing insights for urban air quality  
33 management.

34

## 35 1 Introduction

36 New ~~p~~Particle ~~f~~Formation (NPF) is a critical process happening in the atmosphere, consisting of the formation of molecular  
37 clusters and their growth through the condensation of precursor vapors (~~e.g.~~ Kulmala et al., 2013). These newly formed  
38 particles play a vital role in influencing air quality (Kulmala et al., 2021). Ultrafine particles (UFP), i.e., particles smaller than  
39 100 nm in diameter, can reach the lungs, blood system, and brain, threatening human health (Schraufnagel, 2020; Vallabani et  
40 al., 2023). Moreover, when newly formed particles grow in size, they can interact directly with the solar radiation or be  
41 activated as cloud condensation nuclei (Gordon et al., 2017; Merikanto et al., 2009; Spracklen et al., 2008; Zhao et al., 2024),  
42 affecting the radiative balance of the Earth and, therefore, the climate. WHO recommended the monitoring of UFP in 2021  
43 (WHO, 2021), and, to comply with such recommendation, the European Union enforces their measurements on the member  
44 states with the Ambient Air Quality Directive 2024/2881. European countries must monitor UFP at both urban and rural  
45 supersites, as well as ~~in~~ at UFP hotspots. Specifically, particle number concentration must be measured for particles larger than  
46 10 nm, with no limitation on the maximum size.

47

48 The Po Valley, in northern Italy, is a region of particular interest for studying NPF due to its unique geographical and  
49 environmental characteristics. It is one of the most polluted areas in Europe (EEA, 2019), not only due to the intense and  
50 diverse emissions (Kuenen et al., 2022), but also due to its enclosed position between the Alps and the Apennines, which  
51 favors the accumulation of air pollutants due to the formation of a shallow boundary layer (Vecchi et al., 2004). Previous  
52 research in this area has consistently highlighted the relevance of NPF events. The study by Rodríguez et al. (2005), including  
53 data between June 1999 and December 2000, explored the relation~~ship~~ between aerosol size distributions and air quality in  
54 Ispra, a rural site in the Northern Po Valley, emphasizing the role of NPF in UFP number concentration. Their findings showed  
55 a negative correlation between UFP number concentration and aerosol mass, underlining the weakness of the traditional air  
56 quality metrics, like PM<sub>2.5</sub> and PM<sub>10</sub>, which do not effectively capture UFP pollution. According to Rodríguez et al. (2005),  
57 NPF events predominantly occurred under clean air conditions, often triggered by Foehn wind coming from the north, which  
58 reduced the number of pre-existing particles and created favorable conditions for the new particles to grow. In contrast, polluted  
59 conditions promoted the condensation of vapors on pre-existing particles. A study by Hamed et al. (2007) conducted over three  
60 years at the rural site of San Pietro Capofiume, Po Valley, found that nucleation events occurred on 36% of the days, with the  
61 highest frequency in spring and summer (peaking to ~70% in May and July) and the lowest in winter and autumn. Favorable  
62 conditions for nucleation included higher temperature, wind speed, solar radiation, and SO<sub>2</sub> and O<sub>3</sub> concentrations, while  
63 relative humidity and NO<sub>2</sub> levels were lower during event days. The back trajectory analysis indicated that air masses primarily  
64 originated from the north and east during nucleation events, highlighting the significant impact of atmospheric circulation on  
65 NPF.

66 Supporting the NPF relevance in the area, Kontkanen et al. (2016) reported frequent NPF (86% of days) during a 1-month  
67 summer campaign at the same site. Focusing on sub-3 nm clusters, this study indicated high cluster concentrations also during

68 high condensation sink (CS) episodes and non-NPF events, hinting at a continuous formation of the smallest particles. During  
69 NPF days, cluster formation peaked with the decrease of CS and relative humidity and the increase in boundary layer height  
70 (BLH), highlighting the role of atmospheric dynamics in the process. Sulfuric acid was identified as a potentially relevant  
71 precursor to the NPF process. More recent findings by Cai et al. (2024), including direct measurements of the NPF precursor  
72 vapors, supported these observations, showing that NPF events occurred on approximately 66% of days during a two-month  
73 spring campaign in San Pietro Capofiume, confirming favorable conditions for NPF in this region. During these events, high  
74 concentrations of sulfuric acid ( $8.5 \cdot 10^6 \text{ cm}^{-3}$ ) were detected, underlining its crucial role in NPF, alongside ammonia and  
75 amines. These studies collectively suggest that NPF substantially contributes to the UFP number concentration and overall  
76 pollution levels in this area, underscoring its importance for both regional air quality and climate. All the previously cited  
77 studies, though, refer to rural areas, while none provide a detailed study of NPF in urban areas of the Po Valley.

78  
79 Several factors differentiate rural and urban environments in regard to NPF. The higher CS in urban areas (Bae et al., 2010;  
80 Cai et al., 2024) can suppress NPF, as the available precursor vapors tend to condense onto existing particles rather than  
81 forming new ones (Seinfeld and Pandis, 2016). The availability, chemical composition, and temporal variation of precursor  
82 vapors are also different in rural and urban areas, as they are affected by human activities and local sources, such as traffic.  
83 The work by Nieminen et al. (2018), for example, showed that formation rates generally increase with an increasing  
84 anthropogenic influence in the atmospheric composition, highlighting the importance of anthropogenic vapors in the NPF  
85 process. Urban environments are characterized by various emission sources that release both potential precursor vapors and  
86 particles across a wide size range, largely complicating the observation of NPF. ~~Thus, in~~ such settings, distinguishing between  
87 primary and secondary particles is ~~thus~~ challenging. Therefore, studying NPF in urban areas requires a comprehensive  
88 approach that accounts for the complex interplay of various processes, including emissions, atmospheric chemistry, and  
89 meteorological conditions. Understanding these interactions is essential for accurately characterizing the NPF mechanism in  
90 such environments. Several studies have already been conducted in urban sites across the world, such as the Chinese megacities  
91 (Dai et al., 2023; Guo et al., 2014; Yao et al., 2018) and European cities (Brean et al., 2020; Salma et al., 2011), which are  
92 discussed in Sect. 3.2. Within this context, the city of Milan provides a particularly complex environment for investigating  
93 NPF. As a major metropolitan area within the Po Valley, Milan is characterized by high population density, intense traffic,  
94 and significant industrial activities. Its geographical location further aggravates air quality challenges, as atmospheric  
95 stagnation often leads to the accumulation of pollutants (Vecchi et al., 2004). This combination of factors makes Milan an  
96 important hotspot for studying air quality and the processes driving NPF in urban settings.

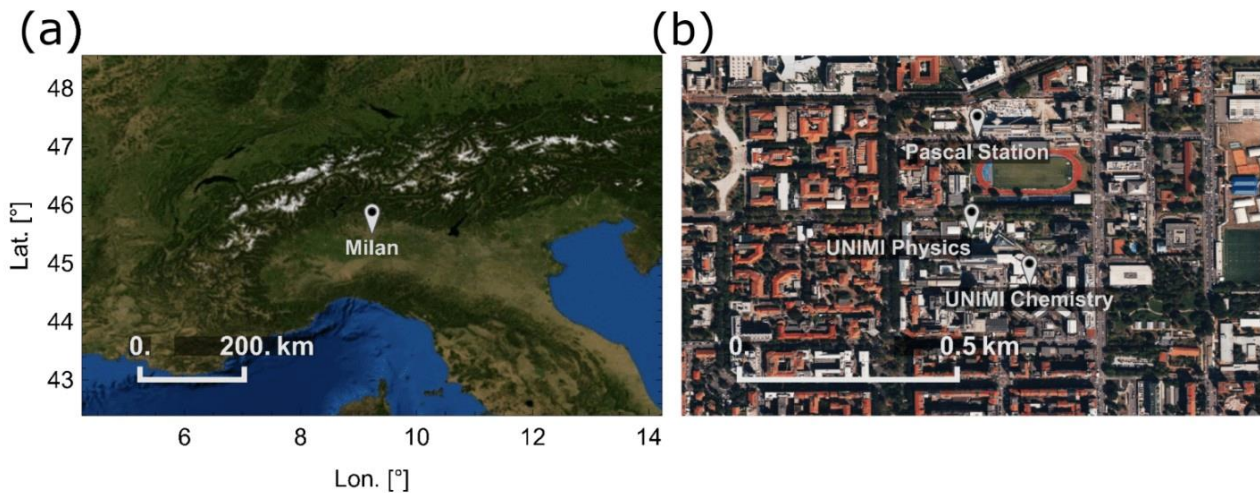
97  
98 In this study, we present a one-year measurement campaign conducted ~~in~~at an urban background site in Milan between the  
99 end of March 2023 and the end of March 2024, as ancillary measurements to the activities foreseen by the European project  
100 Ri-Urbans (<https://riurbans.eu>). The main objective was to quantify the intensity, characteristics, and driving mechanisms of  
101 NPF. By integrating measurements of particle number size distributions, air pollutant concentrations, and meteorological

102 conditions, along with outputs from the FLEXible PARTicle dispersion model (FLEXPART), we investigated the key factors  
103 governing NPF. By presenting a dataset of particle number size distributions extending down to 1.2 nm, we also **evaluated**  
104 **show the importance of extending size distribution measurements below 10 nm, especially in relation to the the influence of**  
105 **the 10 nm cut-off diameter of the** European air quality directive 2024/2881 **\_on reported particle number concentrations in**  
106 **urban Milan.**

## 107 2 Data and methods

### 108 2.1 Location description

109 Milan is located in the Po Valley (Fig. 1a) at the coordinates 45.47°N, 9.19°E, at an altitude of 120 m a.s.l. It is the most  
110 populated city of the Po Valley with a population of ~1.4 million, reaching ~3.2 million when considering the entire  
111 metropolitan area (~~Istat~~ **ISTAT**, 2024). Our measurements were taken in an urban background area, referred to as the Pascal  
112 area (Fig. 1b) due to the presence of the Pascal air quality monitoring station of the regional environmental agency (ARPA  
113 Lombardia). The area is located in the eastern part of the city of Milan, and the instruments were installed at the Physics  
114 (45.4764°N, 9.2317°**WE**) and Chemistry (45.4754°N, 9.2329°**WE**) Departments of the University of Milan (UNIMI). This is  
115 an urban background area, which is affected by several sources of pollution, such as traffic, domestic heating, and transported  
116 industrial and agricultural emissions (Colombi et al., 2023).



117

118 **Figure 1: a) Location of the Po Valley and specifically Milan, in white pin; b) Focus on the Pascal area, where the measurement**  
119 **sites (ARPA Lombardia Pascal ~~Station~~station, Physics Department of UNIMI, and Chemistry Department of UNIMI) are located.**  
120 **The satellite maps were generated using Mathematica 14.1 (Wolfram Research, 2025) with imagery from Bing Maps (Microsoft, last**  
121 **access: April 17<sup>th</sup>, 2025).**

## 122 2.2 Size distribution data

123 Our size distribution measurements were performed with a set of three instruments: a TSI Scanning Mobility Particle Sizer  
124 (SMPS), an Airel Neutral cluster and Air Ion Spectrometer (NAIS), and an Airmodus A11 nano-Condensation Nucleus  
125 Counter (nCNC) system, combining an Airmodus A10 Particle Size Magnifier (PSM) and an Airmodus A20 Condensation  
126 Particle Counter (CPC). The nCNC and the SMPS were located on the second floor of the Chemistry Department of UNIMI  
127 and measured particle number size distributions between 1.2 and 3 nm (Lehtipalo et al., 2022) and between 11 and 480 nm,  
128 respectively. The NAIS measured number size distributions of particles with a diameter between 2.5 and 40 nm and of positive  
129 and negative ions with a diameter between 0.8 and 40 nm (Manninen et al., 2016; Mirme and Mirme, 2013). The instrument  
130 was located on the first floor of the Physics Department of UNIMI, at a distance of about 160m from the nCNC and SMPS  
131 measurements. While the difference in location between the NAIS and the other instruments may have introduced some  
132 uncertainty, all inlets faced the interior of the University's yard, which is not constantly affected by one specific source (for  
133 example, traffic), and can, therefore, be considered representative of Milan urban background. For this reason, the combination  
134 of the data by these instruments was considered reasonable regardless of their different location. -The NAIS measurements  
135 began in March 2023 and ended in ~~March~~ February 2025, while those of the nCNC and the SMPS started in May 2023 and  
136 ended in ~~April~~ March 2024. The particle number size distribution data between March 27<sup>th</sup>, 2023, and March 26<sup>th</sup>, 2024, were  
137 used for this study.

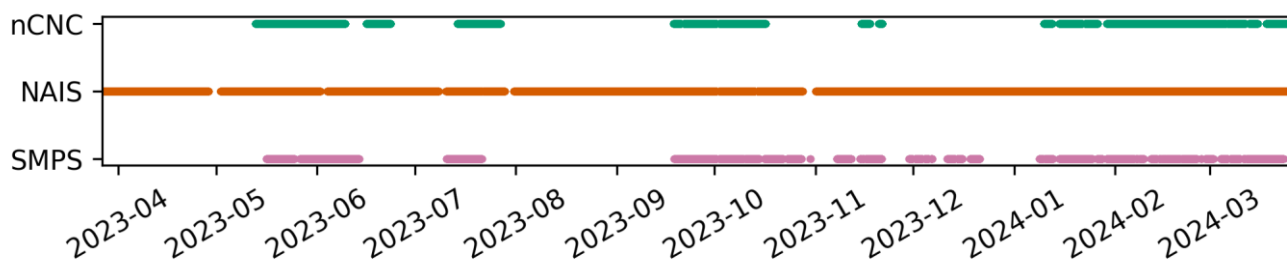
138 Considering the high number concentration of sub-3nm particles in the city, the nCNC was equipped with an Airmodus  
139 Nanoparticle Diluter (AND; Lampimäki et al., 2023) running with a dilution factor of 5 and measuring instrumental  
140 background automatically three times a day for 8 minutes. The system was run with a core sampling inlet, as integrated into  
141 the AND designed. Using a dry flow for the dilution, the AND also acted as a dryer. The AND inlet consisted of a 40 cm  
142 stainless steel tube sampling ambient air at a flow rate of about 6 L min<sup>-1</sup>, while the PSM, connected to the AND through a  
143 conductive tube, worked with a flow rate of 2.5 L min<sup>-1</sup>. The nCNC measured in scanning mode with saturator flow scanning  
144 between 0.1 L min<sup>-1</sup> and 1.3 L min<sup>-1</sup>. Each scan lasted 4 minutes. To guarantee the correct functioning of the instrument,  
145 several checks and cleaning procedures were applied. Every week, both the PSM and the CPC were drained, and their  
146 connection was cleaned with isopropanol and compressed air. The involved flows and the background were also manually  
147 checked. Flushing of the PSM was performed once every two weeks, while the inlet line was cleaned once a month. The overall  
148 status of the instrument was checked almost every day. The data from the nCNC were inverted using the kernel inversion  
149 method and applying the corrections for the background, the detection efficiency, the dilution factor, and the inlet losses,  
150 estimated to be between 20 and 9.3%, depending on the particle size (Lehtipalo et al., 2022).

151 The SMPS (Wang and Flagan, 1990), consisting of a 3080 TSI classifier, a 3081 TSI DMA, and a 3772 TSI CPC, was equipped  
152 with a stainless steel inlet drawing 1 L min<sup>-1</sup> of ambient air, a 4.9 kV X-ray tube to provide particles with a known charge  
153 distribution, and with a silica gel dryer to reduce the relative humidity of the air sample. The DMA scanned between ~10 V  
154 and ~9700 V during a cycle of 3 minutes, producing size distributions between 11 nm and 480 nm. Weekly checks of the

155 performance of the instrument included CPC draining and flow checks. The inlet line was cleaned once a month with  
156 isopropanol and the silica gel was regenerated when needed. The data were inverted using the TSI Aerosol Instrument Manager  
157 program. The data were corrected for counting errors due to multiple charging.

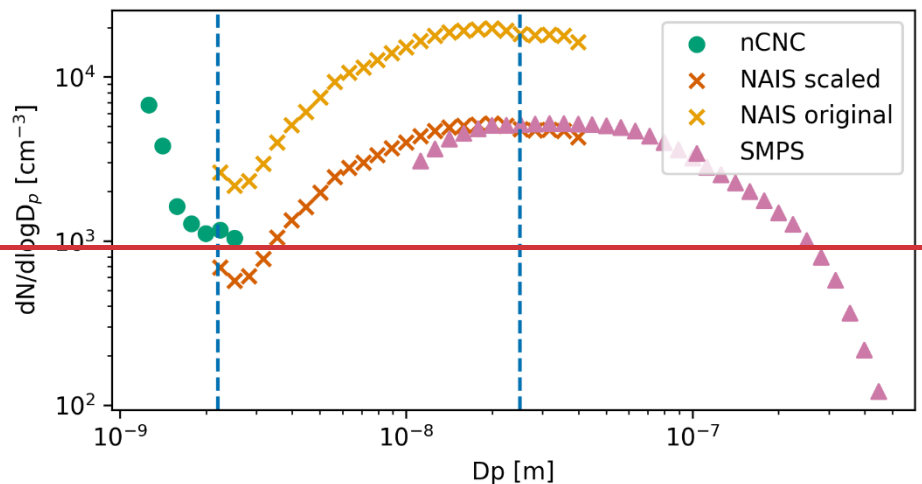
158 The NAIS was equipped with a 50 cm copper inlet followed by a downward bend to prevent rain from entering the instrument,  
159 resulting in a total inlet length of approximately 60 cm. Ambient air was sampled at a flow rate of 54 L min<sup>-1</sup>. The NAIS  
160 instrument measured in particle, ion, and offset mode, changing mode every 90 seconds. Considering the high inlet flow rate  
161 of the NAIS, drying the sample flow was not possible. Instrument cleaning was performed when needed. The measured data  
162 were inverted automatically by the Spectop software following the procedure described by Mirme and Mirme (2013). The data  
163 were then corrected for inlet losses (between 15% and 0.1%, depending on the particle size; Gormley and Kennedy, 1948) and  
164 ion calibration (Wagner et al., 2016). The final particle number size distributions were obtained by averaging those from the  
165 positive and negative columns.

166 Figure 2 illustrates the data availability throughout the campaign. Of all the instruments, the NAIS provided the most  
167 comprehensive data coverage, recording data on approximately 9795% of the campaign daytime. On the other hand, the  
168 nCNC and SMPS recorded data for about 4240% and 4542% of the daytime, respectively. Measurement gaps mostly resulted  
169 from technical challenges, including high summer temperatures, power outages, CPC flooding, and delays in equipment  
170 shipments.

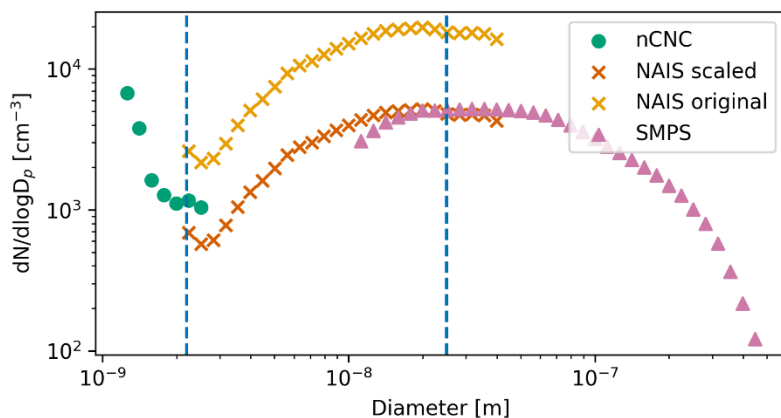


171  
172 **Figure 2: Particle number size distribution data availability throughout the campaign.**

173 The total size distributions were obtained by combining the nCNC, NAIS, and SMPS data. First of all, all the data were  
174 resampled to a 15-minute time resolution and rebinned to a diameter resolution of 0.05 in log10 scale. Then, the median size  
175 distributions of the three instruments were compared for the periods when all three instruments were operating simultaneously  
176 (Fig. 3). A scaling factor of 3.8 was applied to the NAIS data, following the approach proposed by Dada et al. (2023). The  
177 scaling factor was obtained by comparing the NAIS and SMPS data in the overlapping size region. during the full measurement  
178 period. Then, the number size distributions from the three instruments were combined using the concentrations measured by  
179 the nCNC for the particles smaller than 2.2 nm, by the NAIS for the particles in the 2.2-25 nm size range, and by the SMPS  
180 for the particles larger than 25 nm. Then, the size distributions of the three instruments were combined at 2.2 nm and 25 nm.  
181 Using the SMPS as a reference instrument, an artifact at the connection between the nCNC and the NAIS data was created.



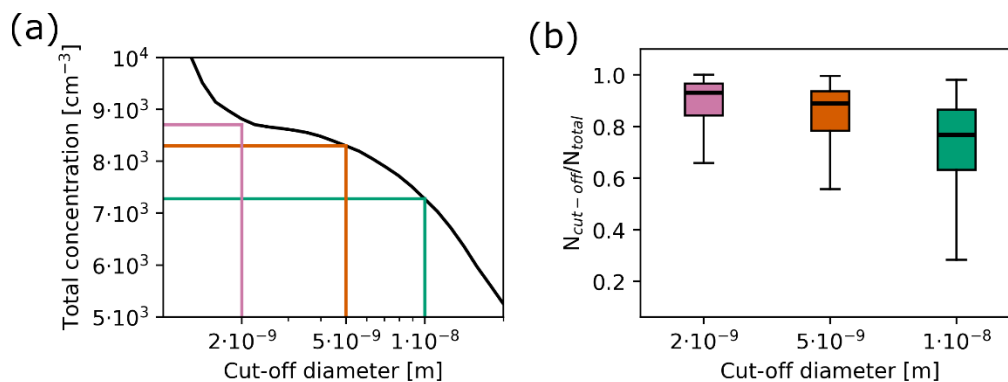
182



183

184 **Figure 3: Median particle number size distributions measured by the nCNC, the NAIS (original and scaled), and the SMPS. The**  
 185 **medians were calculated using only the periods when all the instruments were measuring simultaneously. The blue vertical lines**  
 186 **mark the diameters at which the size distributions were combined.**

187 The relevance of UFP has led the European Union to enforce the measurement of their number concentration. As reported in  
 188 Sect. 1, a 10 nm cut-off was chosen to define UFP. In Fig. 4, the total particle number concentration for different cut-off sizes  
 189 was calculated by integrating the size distribution from different lower limits (2 nm, 5 nm, and 10 nm) to the upper limit of  
 190 480 nm. In our dataset, lowering the threshold from 10 nm to 5 nm would result in an average increase of 14%, whereas  
 191 adopting a 2 nm cut-off would lead to a 19% increase (Fig. 4a). Fig. 4b shows the variability of the ratio between the  
 192 concentration for a certain cut-off size (2, 5, 10 nm) and the total particle number concentration. These considerations highlight  
 193 the potential impact of measurement thresholds on reported UFP number concentrations and emphasize the importance of  
 194 detailed measurements of sub-10 nm particles. While the availability and complexity of the instrumentation pose significant  
 195 challenges to measuring sub-10 nm particles, the dataset presented in this work demonstrates the value of extending the  
 196 measurements below 10 nm.



197

198 Figure 4: a) Total particle number concentration for different cut-off sizes, averaged over the entire campaign time. The green line  
 199 marks the cut-off diameter of 10 nm, the orange one of 5 nm, and the pink one of 2 nm; b) boxplots representing the ratio between  
 200 the concentration for different cut-off diameters ( $N_{\text{cut-off}}$ ) and the total particle number concentration ( $N_{\text{total}}$ ). In each boxplot, the  
 201 box represents the interquartile range, between the 25<sup>th</sup> and the 75<sup>th</sup> percentile, and the median (50<sup>th</sup> percentile) is shown as a  
 202 horizontal line inside the box. The whiskers of the boxplot extend from the edges of the box to the smallest and largest values within  
 203 1.5 times the interquartile range. Outliers are not shown in this figure.

### 204 2.3 Complementary data

205 The study ~~included~~ used meteorological and air pollutant concentration data provided by ARPA Lombardia, the regional  
 206 environmental agency responsible for managing multiple monitoring stations across the area. For the analysis, data from the  
 207 Pascal station, situated approximately 250 m from the UNIMI buildings, were utilized. The meteorological dataset included  
 208 variables such as atmospheric temperature, wind speed and direction, radiation, and relative humidity. The pollutant  
 209 concentrations included PM<sub>10</sub>, PM<sub>2.5</sub>, NO<sub>2</sub>, SO<sub>2</sub>, O<sub>3</sub>, NO<sub>x</sub>, ammonia, and equivalent black carbon- (eBC, Savadkoohi et al.,  
 210 2024) concentrations.

211 ARPA Lombardia also provided BLH data from the nearby station of Milano Parco Nord. The BLH was estimated using the  
 212 Gryning-Batchvarova model for the daytime convective boundary layer (Batchvarova and Gryning, 1991) and the Zilitinkevich  
 213 model for the nocturnal stable boundary layer (Zilitinkevich and Baklanov, 2002). Both models used turbulence variables that  
 214 were measured by ARPA Lombardia with a triaxial ultrasonic anemometer at the Milano Parco Nord station. The choice of  
 215 the appropriate model was based on the assessment of the boundary layer stability, determined from the sensible heat flux,  
 216 also measured by the ultrasonic anemometer at the same site.

217 Briefly, the Gryning-Batchvarova model describes the daytime convective boundary layer using a simplified analytical  
 218 approach. The profiles of the main variables are schematized considering that, throughout the boundary layer, each variable  
 219 assumes a constant value equal to its vertical mean, the entrainment layer is considered to be of infinitesimal thickness, and  
 220 that, at the entrainment layer, there is a characteristic discontinuity for each variable. For the assessment of the stable boundary  
 221 layer, (Zilitinkevich et al., (2007) developed theoretical models considering simple equilibrium regimes in a step-by-step  
 222 approach. They applied Large Eddy Simulation to validate their theoretical multi-limit BLH formulation, which reduces to  
 223 known asymptotic limits in the neutral and nocturnal stable regime. Indeed, the stable and neutral BLH evolution is controlled

224 ~~by factors (e.g., baroclinic shear, large-scale vertical velocity at the top of the boundary layer, non-stationarity of the boundary~~  
225 ~~layer and its horizontal heterogeneity) that are difficult to measure and to use for the validation of the theory. ARPA Lombardia~~  
226 ~~also provided BLH data for the nearby station of Milano Parco Nord. The BLH was estimated using data from ultrasonic~~  
227 ~~anemometers, applying the Gryning-Batcharova model for convective boundary layer (Batchvarova and Gryning, 1991) and~~  
228 ~~the Zilitinchevich model for stable boundary layer (Zilitinkevich and Baklanov, 2002). All data were recorded with an hourly~~  
229 ~~time resolution.~~

230 All data were provided with an hourly time resolution.

231 Using these datasets, we calculated the daily ventilation index (VI), which reflects the potential of pollutants to disperse  
232 efficiently through proper ventilation. For each day, this index is defined as:

$$233 \quad VI = \text{mean}(ws) \cdot \max(BLH), \quad (1)$$

234 where  $ws$  is the wind speed, and  $BLH$  is the boundary layer height during that day.

235 In line with ARPA Lombardia guidelines, a VI value of  $400 \text{ m}^2 \text{ s}^{-1}$  was used as threshold to identify stagnant days.

## 236 **2.4 Tools and parameters**

### 237 **2.4.1 Nano-particle ranking**

238 The NPF occurrence was ~~analyzed-assessed~~ through the n Nano-particle ranking analysis (Aliaga et al., 2023). This method  
239 provides an automated, continuous, and objective way of analyzing NPF compared to the manual NPF classification based on  
240 the visual inspection of the data and on the identification of a few discrete classes (Dal Maso et al., 2005). The method consists  
241 in assessing the intensity and probability of NPF using the change in the concentration of 2.5-5 nm particles during each day.  
242 The total concentration of 2.5-5 nm particles from the NAIS,  $N_{2.5-5}$ , was used to identify the NPF active and background time  
243 windows as described by Aliaga et al. (2023), paying particular attention to minimize the impact of traffic rush hours from the  
244 active time period, considering that Milan is an urban site. The active region was defined as between 10 and 16 Central  
245 European Time (UTC+1), and the background between 23 and 5 Central European Time (UTC+1). The ranking value  
246 ( $\Delta N_{2.5-5}$ ) for day  $i$  was, then, calculated as follows:

$$247 \quad \Delta N_{2.5-5,i} = \max(N_{2.5-5,i_{active}}) - \text{median}(N_{2.5-5,i_{background}}). \quad (2)$$

248 The ranking values were then ordered according to their magnitude to determine the percentile rank of each day. The percentile  
249 rank of each day indicates the proportion of days with lower  $\Delta N_{2.5-5}$  than the value of such day. Therefore, the days with a  
250 lower percentile rank have lower  $\Delta N_{2.5-5}$ , indicating weaker NPF than those with higher percentile rank.

### 251 **2.4.2 Model simulation**

252 The Weather Research and Forecasting (WRF) model (v3.71), a regional meteorological model, was employed in this study.  
253 The model was driven by ~~the data~~ data from the National Centers for Environmental Prediction (NCEP) Climate Forecast  
254 System (CFSv2), with a temporal resolution of 6 hours and a horizontal resolution of  $1^\circ$ . For the simulation, the WRF model

255 was configured over a domain with a spatial resolution of  $18 \times 18 \text{ km}^2$  (Fig. S1) centered on Milan and roughly covering  
 256 Europe. WRF simulations were performed using the Rapid Radiative Transfer Model radiation scheme (Mlawer et al., 1997),  
 257 the Thompson aerosol-aware microphysics scheme (Hong et al., 2004), the Monin-Obukhov surface-layer scheme (Janjic,  
 258 2003), and the NOAA Land Surface Model scheme (Chen and Dudhia, 2001). The Mellor-Yamada-Janjic turbulent kinetic  
 259 energy (TKE) scheme (Janjic, 1994) was chosen to assess the boundary layer. WRF simulations were performed on 33 vertical  
 260 sigma layers. Annual anthropogenic emission fluxes for  $\text{SO}_2$  and  $\text{NO}_x$  (see for example, the map of  $\text{NO}_x$  emissions in Fig. S2)  
 261 were retrieved from the CAMS datasets at  $0.1 \times 0.1^\circ$  (around 10 km) horizontal resolution and distributed hourly over the  
 262 investigated period, with temporal profiles based on the EMEP MSC-W model (Simpson et al., 2012). The FLEXPART  
 263 (FLEXible PARTicle dispersion) model, a Lagrangian particle dispersion model, was used to simulate particle transport in the  
 264 backward direction. In this study, we utilized version 3.3.2 of FLEXPART (Brioude et al., 2013) for backward dispersion to  
 265 identify the source regions of the air masses reaching Milan. The model was driven by the meteorological data generated from  
 266 the WRF simulation, with input provided at a temporal resolution of 15 minutes. The FLEXPART domain was aligned with  
 267 the resolution and extent of the WRF domain. The vertical structure of the domain included 12 levels, spanning from ground  
 268 level to an altitude of 9000 meters. To conduct the simulation, 10000 particles were released every hour from Milan over the  
 269 period between April 1<sup>st</sup>, 2023, and March 31<sup>st</sup>, 2024. These particles, treated as passive tracers, were emitted from an altitude  
 270 between 0 to 100 meters above ground level within an  $18 \times 18 \text{ km}^2$  area centered on the city. Their trajectories were traced  
 271 backward in time for up to 72 hours. The backward-mode output from FLEXPART provided the sSource-rReceptor  
 272 rRelationship (SRR), expressed in units of s, which represents the relative residence time of the particles within each grid cell,  
 273 offering insights into the contribution of specific regions to the air masses arriving in Milan.

### 274 2.4.3 Condensation sink

275 The cCondensation sSink (CS) refers to the rate at which vapors condense onto pre-existing particles in the atmosphere. The  
 276 CS is influenced by the diffusivity of the condensing molecules, the size distribution of the particles, and the environmental  
 277 conditions (Kulmala et al., 2012). It is estimated as:

$$278 \quad CS = 4\pi D \sum_{d'_p} \beta_{m,d'_p} d'_p N_{d'_p}, \quad (3)$$

279 where  $D$  is the diffusion coefficient of the condensing vapor in the air (sulfuric acid was assumed),  $d'_p$  the particle diameter,  
 280 and  $N_{d'_p}$  the concentration of particles with diameter  $d'_p$ .  $\beta_m$  was calculated using the Fuchs-Sutugin approximation (Fuchs  
 281 and Sutugin, 1971). The CS was calculated only when both NAIS and SMPS data were available, using the original data  
 282 without making assumptions about water. This introduces some uncertainty in the CS values as the NAIS measured a wet flow  
 283 while the SMPS one was dried.-

#### 284 2.4.4 Formation rate

285 The formation rate (J) refers to the rate at which new particles appear in a given size range due to nucleation, growth into that  
286 size range, or emissions. If the selected size is small enough, it can be assumed that NPF is the main process forming new  
287 particles, although the contribution of traffic emissions cannot be excluded in urban environments (Rönkkö et al., 2017).  $J_{1.5}$ ,  
288  $J_3$ , and  $J_7$  were calculated according to the following definition (Kulmala et al., 2012) for the days with a complete size  
289 distribution:

$$290 J_{d_p} = \frac{dN_{d_p}}{dt} + CoagS_{d_p}N_{d_p} + \frac{GR}{\Delta d_p} N_{d_p}, \quad (4)$$

291 where  $CoagS_{d_p}$  is the coagulation sink at size  $d_p$ ,  $GR$  is the growth rate and  $N_{d_p}$  is the particle number concentration at size  
292  $d_p$ . Particle number concentrations in the 1.5-3 nm, 3-7 nm, and 7-20 nm size ranges were used to calculate  $J_{1.5}$ ,  $J_3$ , and  $J_7$ ,  
293 respectively.

294 The coagulation sink is the rate at which particles are lost due to coagulation with pre-existing particles (Kulmala et al., 2012):

$$295 CoagS_{d_p} = \sum_{d'_p=d_p}^{d'_p=d_{pmax}} K(d_p, d'_p)N_{d'_p}, \quad (5)$$

296 where  $K(d_p, d'_p)$  is the coagulation coefficient between particles of diameter  $d_p$  and  $d'_p$ .

297 The growth rate (GR) indicates the rate at which particles increase in size over time. Considering the limited variability of  
298 its values (Kulmala et al., 2022), the GR was estimated using the daily median size distribution surface plot calculated over all  
299 days with NPF rank above the 80<sup>th</sup> percentile. The GR was computed for the size ranges of 3-7 nm, 7-20 nm, and 20-100 nm  
300 with the maximum concentration method (Kulmala et al., 2012) to evaluate  $J_{1.5}$ ,  $J_3$ , and  $J_7$ , respectively (Kerminen et al.,  
301 2018). Considering the limited variability of the GR values (Kulmala et al., 2022), the median size distribution of the days  
302 above the 80<sup>th</sup> percentile rank was used to calculate the average GR in the size ranges of 3-7 nm, 7-20 nm, and 20-100 nm  
303 with the maximum concentration method (Kulmala et al., 2012) to evaluate  $J_{1.5}$ ,  $J_3$  and  $J_7$  respectively (Kerminen et al., 2018).  
304 -The GR values were calculated using a size interval around the upper limit of the one used for the J calculation, in order to  
305 estimate the growth out of the size bin.

306 The uncertainty associated with this method for the estimation of GR and J is discussed in the Supplementary Materials.

#### 307 2.4.5 Sulfuric acid proxy calculation

308 A proxy for sulfuric acid concentration was calculated using the approach described by Dada et al. (2020). The equation for  
309 the concentration of sulfuric acid in an urban site was used (Dada et al., 2020):

$$310 [H_2SO_4] = -\frac{CS}{2 \cdot (9.9 \cdot 10^{-9})} + \left[ \left( \frac{CS}{2 \cdot (9.9 \cdot 10^{-9})} \right)^2 + \frac{[SO_2]}{9.9 \cdot 10^{-9}} (1.6 \cdot 10^{-9} \cdot GlobRad) \right]^{1/2}, \quad (6)$$

311 where  $[SO_2]$  is the  $SO_2$  concentration,  $GlobRad$  is the global radiation, and  $CS$  is the condensation sink.

## 312 2.4.6 Air mass exposure

313 To investigate the impact of the air masses on NPF, we adapted the ~~a~~Air ~~m~~Mass ~~e~~Exposure (AME) methodology originally  
314 proposed by Hakala et al. (2022). In their method, AME calculations combined FLEXPART output with static two-  
315 dimensional fields to identify when air masses were exposed to different pollutant emissions.

316 In this study, we modified the AME calculation by incorporating FLEXPART output with three-dimensional emissions  
317 (calculated as mentioned in section 2.4.2), including temporal variations, following the approach used by Bettineschi et al.  
318 (2025).~~by incorporating FLEXPART output with dynamic, three dimensional emissions data from the CHIMERE model,~~  
319 ~~including its temporal variations.~~ For each particle release event, we computed the AME for a specific pollutant or substance  
320  $x$  (denoted as  $AME_x$ ) using emission data for that substance derived from the emission model (emiSURF) output. This  
321 approach allowed us to account for the temporal variability of emissions within air masses, enabling a more precise evaluation  
322 of the exposure of air masses to pollutant emissions.

323 Given a domain  $\Omega$ , containing time ( $t$ ), height ( $h$ ), longitude ( $x$ ) and latitude ( $y$ ) as coordinates, and a release time ( $\tau$ ), the  
324  $AME_x$  for a specific  $\tau$  is calculated according to the following equation:

$$325 \quad AME_x(\tau) = \sum_{(t,x,y) \in \Omega} \sum_{h=0}^{500m} SRR(t, x, h, y; \tau) \cdot X(t, x, y). \quad (7)$$

## 326 2.4.7 Air mass trajectories description

327 To clearly visualize the origin of the air masses, the trajectory density was defined as the absolute difference between the  
328 percentage of trajectories passing over each grid cell, regardless of their height, and arriving in Milan on days with ~~a~~a-NPF rank  
329 above the 80<sup>th</sup> percentile, and the percentage of all trajectories passing over the same area:

$$330 \quad \Delta\%T = \%T_{>80} - \%T_{tot}. \quad (8)$$

331 Specifically,

$$332 \quad \%T_{>80}(x, y) = \frac{\sum_{\tau \in T_{80}} \delta(\tau; x, y)}{N_{80}}, \quad (9)$$

333

$$334 \quad \%T_{tot}(x, y) = \frac{\sum_{\tau \in \Omega} \delta(\tau; x, y)}{N_{tot}}, \quad (10)$$

335 where  $T_{80}$  is the set of releases arriving when the ~~ranking~~-percentile ~~rank~~ is larger than 80,  $N_{80}$  is the total number of these  
336 releases,  $N_{tot}$  is the total number of releases and,  $\delta(\tau; x, y)$  assumes 1 or 0 values as follows:

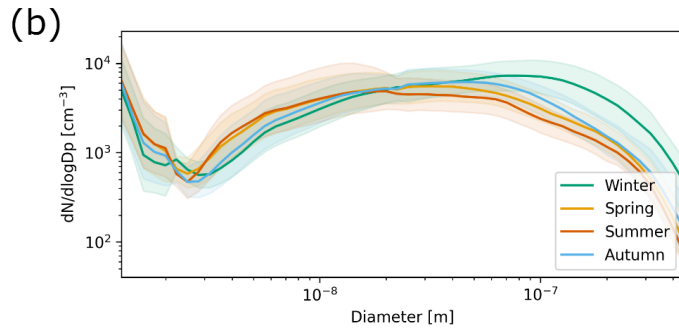
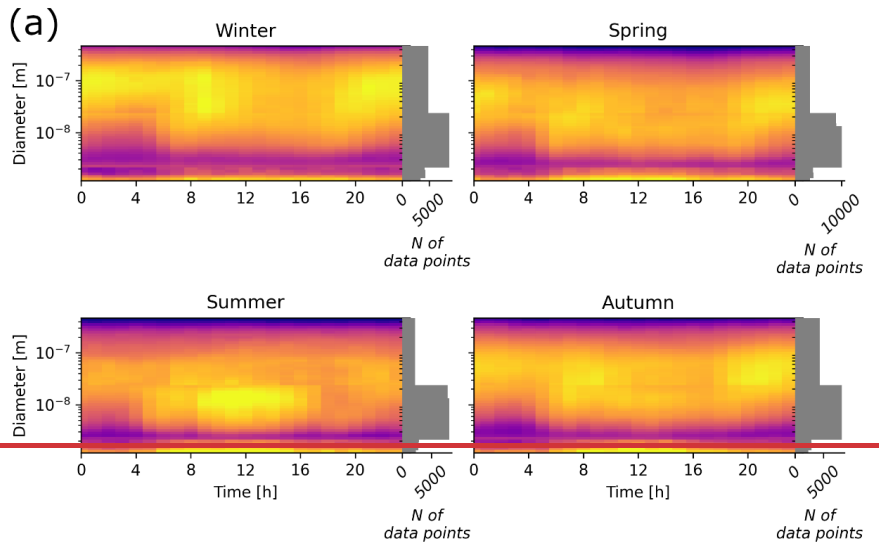
$$337 \quad \delta(\tau; x, y) = \begin{cases} 1 & \text{if } \sum_{(t,h) \in \Omega} SRR(t, h; x, y, \tau) > 0 \\ 0 & \text{otherwise} \end{cases}. \quad (11)$$

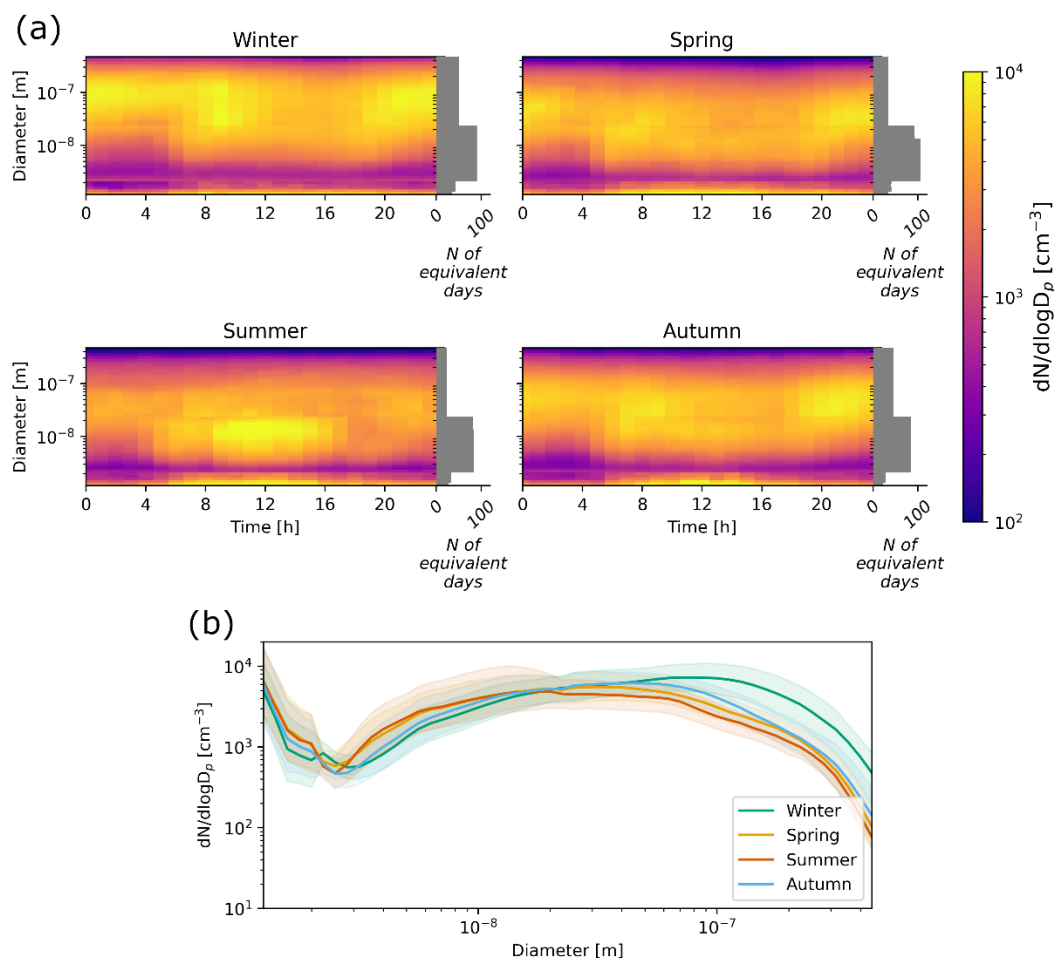
338 This means that  $\delta(\tau; x, y) = 1$  if, for a given release, at least one of the 10000 released particles passed through the point  
339  $(x, y)$  during the previous 72 hours.

### 340 3 Results and discussion

#### 341 3.1 Size distributions characterization

342 The particle number size distributions in Milan exhibited a clear seasonal cycle, which is illustrated in Fig. ~~4a-5a~~ and Fig. ~~4b~~  
343 ~~5b~~ through the daily average-median size distribution surface plot per season and the average-median size distribution per  
344 season, respectively. The months of December, January, and February were included in winter; March, April, and May in  
345 spring; June, July, and August in summer; September, October, and November in autumn.





347

348 **Figure 45: a) Daily median particle number size distribution surface plot per season. The bar plots report the number of equivalent**  
 349 **days used to calculate the medians, computed as the total number of 15-minute data points divided by 96 (the number of 15-minute**  
 350 **intervals in one day). The grey bar plots represent the number of data points available for each diameter. Times are in Central**  
 351 **European Time, UTC+1; b) Median-median particle number size distribution per season. The shaded areas represent the**  
 352 **interquartile ranges.**

353 During winter, the highest concentrations of particles larger than 50 nm were observed (Fig. 4b5b). This increase was probably  
 354 the result of both a decrease in the BLH and an increase in biomass burning emissions (Colombi et al., 2023). Moreover, the  
 355 typical traffic-related pattern was evident, with marked increases across all particle size ranges starting from 5:00 and 17:00  
 356 Central European Time, UTC+1 (Fig. 4a5a), coinciding with the morning and evening rush hours.

357 In spring, and particularly in summer, these traffic-related peaks became less pronounced, suggesting an increase in the  
 358 atmospheric mixing. Additionally, the data revealed a clear midday increase in sub-10 nm particles (Fig. 4a5a), which was  
 359 most likely associated with NPF events. This phenomenon, which became more pronounced in the warmer months, was driven  
 360 by photochemical reactions, enhanced by higher solar radiation and it was, therefore, mostly observed during spring and

361 summer. During summer, we observed the most significant increase in sub-10 nm particle number concentrations, alongside  
362 the lowest levels of particles larger than 100 nm (Fig. 4b5b).

363 In autumn, the traffic-related peaks reappeared (Fig. 4a5a) due to the combined effect of the increase in traffic emissions  
364 (Colombi et al., 2023) and the decrease in atmospheric dispersion and BLH, becoming again a more dominant factor  
365 influencing particle number concentrations. However, the median concentrations across all particle sizes during autumn  
366 remained similar to those observed in spring, indicating a seasonal transition towards winter. Overall, though, considering the  
367 discontinuities in the data collection (Fig. 2) and the definition of each season, these conclusions may not be representative of  
368 each entire season and their comparison has intrinsic uncertainties.

369 The shape and values of the median size distributions in Fig. 4b-5b are in agreement with those ~~of-reported for~~ other urban  
370 background sites of southern, central, and eastern Europe (Trechera et al., 2023). The comparison between the characteristics  
371 of the size distribution surface plots per season (Fig. 4a5a) in Milan and other urban background sites (Trechera et al., 2023)  
372 also does not point out any anomaly. As observed in Milan, several other urban background sites across Europe showed a more  
373 pronounced increase in sub-25 nm particles at midday during the warmer months. Higher concentrations in the same size range  
374 due to traffic rush hours were also ~~reported-recorded~~ in all urban background sites (Trechera et al., 2023).

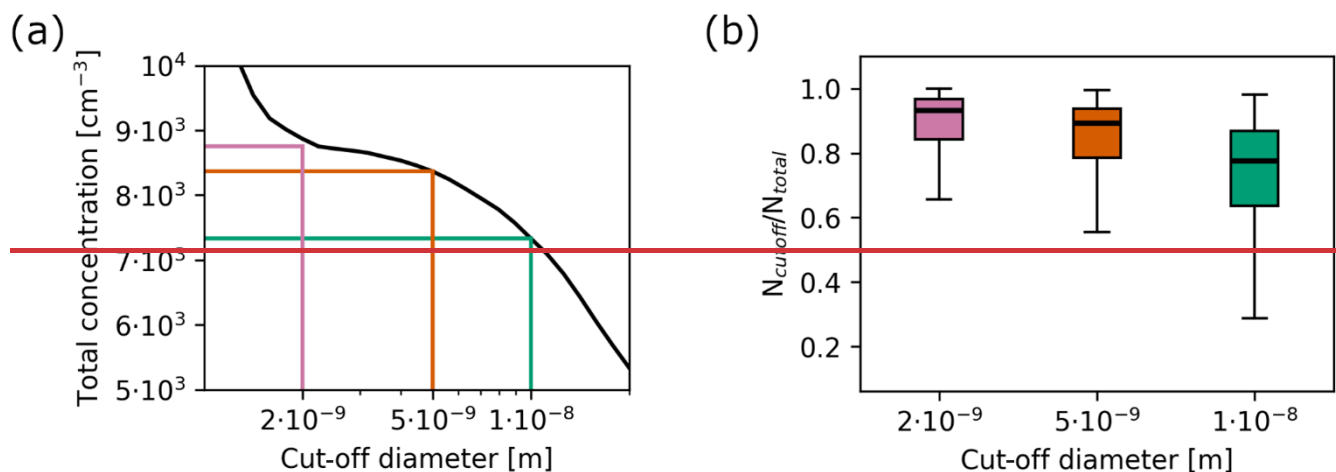
375 Other than this qualitative comparison, a quantitative one was also performed, and the concentrations in the nucleation, Aitken,  
376 and accumulation modes measured in Milan were compared with the values reported for other European cities. The average  
377 number concentrations for particles in the 10-25, 25-100, and 100-480 nm size ranges were 2642 cm<sup>-3</sup>, 4080 cm<sup>-3</sup>, and 1819  
378 cm<sup>-3</sup>, respectively. Regarding the accumulation mode, Milan fell within the typical southern European cities, characterized by  
379 high concentrations of particles in this size range. The Aitken mode in Milan exhibited a lower average concentration compared  
380 to other southern European cities (4800-5900 cm<sup>-3</sup>), but lay at the upper end of the range reported for central European cities,  
381 characterized by intermediate concentrations in this mode. Finally, intermediate concentration values were recorded in the  
382 nucleation mode in Milan.

383 This comparison, though, should be interpreted with caution as it may be affected by several uncertainties. In fact, while the  
384 data presented by Trechera et al. (2023) refer to the years 2017-2019, the data presented in this study cover a single year (2023-  
385 2024), characterized by several gaps in the data availability, affecting especially the calculations in the Aitken and  
386 accumulation modes. Moreover, differences in the instruments cut-off diameters may further bias this comparison.

387 The ratio between the average particle number concentration in the nucleation mode ( $N_{10-25}$ ) and eBC was used to qualitatively  
388 assess the relative contributions of primary and secondary emissions in Milan compared to other European urban background  
389 sites. Milan exhibited an intermediate-low  $N_{10-25}/eBC$  ratio ( $\sim 1444 \text{ cm}^{-3} \mu\text{g}/\text{m}^3$ ), within the approximate range of 900-4500  
390 calculated for other cities (Trechera et al., 2023). This suggests that primary emissions (traffic) dominated the nucleation mode  
391 particles in Milan, whereas in other European sites, photochemistry played a more significant role.

392 Considering that we measured size distributions ranging from 1.2 nm to 480 nm, it is relevant to evaluate the implications of  
393 the 10 nm cut off established by the European Union for the measurement of UFP. In Fig. 5, the total particle number  
394 concentration at different cut off sizes was calculated by integrating the size distribution from different lower limits (2 nm, 5

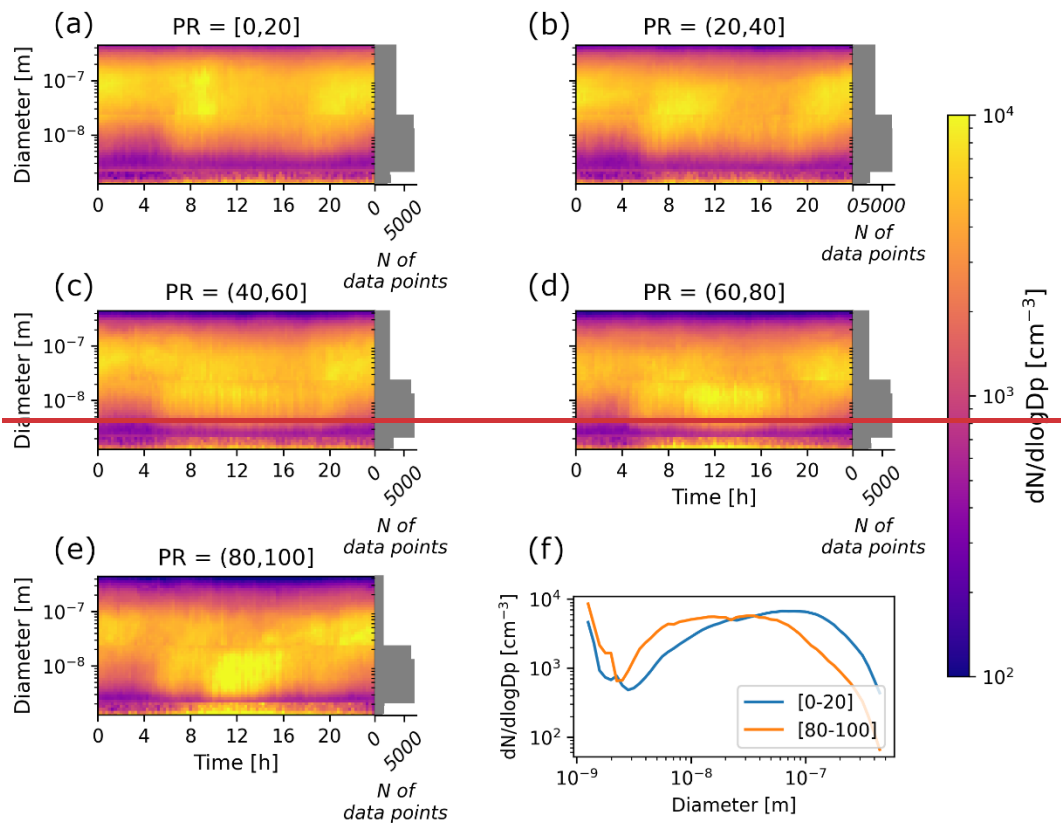
395 nm, and 10 nm) to the upper limit of 480 nm. While the availability and complexity of the instrumentation pose significant  
 396 challenges to measuring sub-10 nm particles, it is important to explore how much the total concentration is underestimated  
 397 due to the chosen cut-off size (Fig. 5a). For instance, in our dataset, lowering the threshold from 10 nm to 5 nm would result  
 398 in an average increase of 14%, whereas adopting a 2 nm cut-off would lead to a 19% increase. Fig. 5b shows the variability of  
 399 the ratio between the concentration for a certain cut-off size (2, 5, 10 nm) and the total particle concentration. These  
 400 considerations highlight the potential impact of measurement thresholds on reported UFP concentrations and emphasize the  
 401 need for further discussion on optimal cut-off values and for improvements in sub-10 nm size distribution measurements.



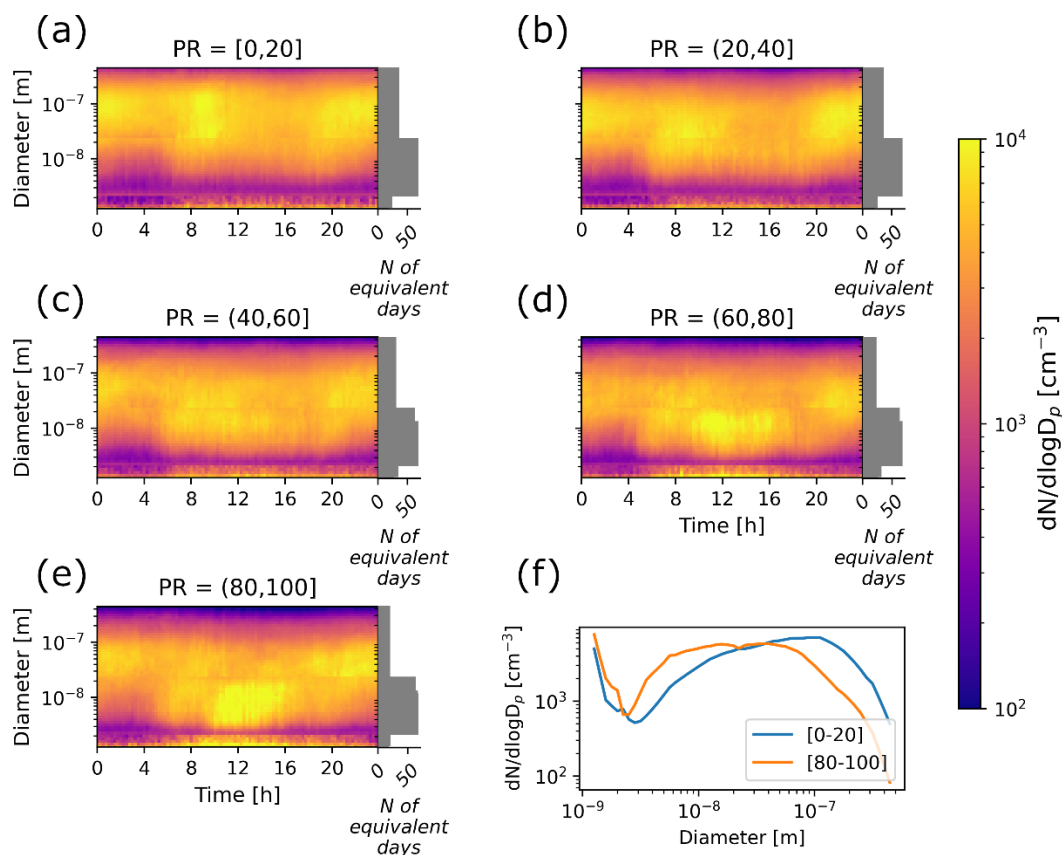
402  
 403 **Figure 5:** a) Total particle number concentration at different cut-off sizes, averaged over the whole campaign time. The green line  
 404 represents the cut-off diameter of 10 nm, the orange one of 5 nm, and the pink one of 2 nm. b) Box plots representing the ratio  
 405 between the concentration at different cut-off diameters ( $N_{\text{cut-off}}$ ) and the total particle concentration ( $N_{\text{total}}$ ). The box plots display  
 406 the interquartile range, between the 25<sup>th</sup> and the 75<sup>th</sup> percentile, and the median (50<sup>th</sup> percentile) as a horizontal line inside the box.  
 407 The whiskers of the box plot extend from the edges of the box to the smallest and largest values within 1.5 times the interquartile  
 408 range. Outliers are not shown in this figure.

### 409 3.2 NPF analysis

410 The Nano-particle ranking analysis was applied to characterize NPF. At higher percentile ranks, a midday increase in particle  
 411 number concentration across all size ranges became clear, indicating NPF (Fig. 6). The process was marked by an initial rise  
 412 in 1.2 nm particle number concentration, followed by an increase in the concentration of larger particles. This pattern indicates  
 413 that NPF occurred over a wide area, including Milan itself. At lower percentile ranks, higher concentrations associated with  
 414 traffic rush hours were evident, but they gradually faded at higher percentile ranks (Fig. 6, panels a to e). This pattern aligned  
 415 with the seasonal variations in particle size distributions and NPF (Fig. S3S4, Fig. 4a5a). In fact, lower ranking values  $\Delta N_{2.5-5}$ ,  
 416 corresponding to weaker NPF, were more frequent during winter (December to February, Fig. S3S4), when traffic peaks were  
 417 also more evident (Fig. 4a5a). Conversely, the strongest NPF events were observed in April and mid-to-high rank values  
 418  $\Delta N_{2.5-5}$  days (percentile ranks between 60 and 80) occurred predominantly between June and August (Fig. S3S4), when  
 419 stronger atmospheric dispersion minimizes the concentration of traffic-related peaks (Fig. 4a5a).



420

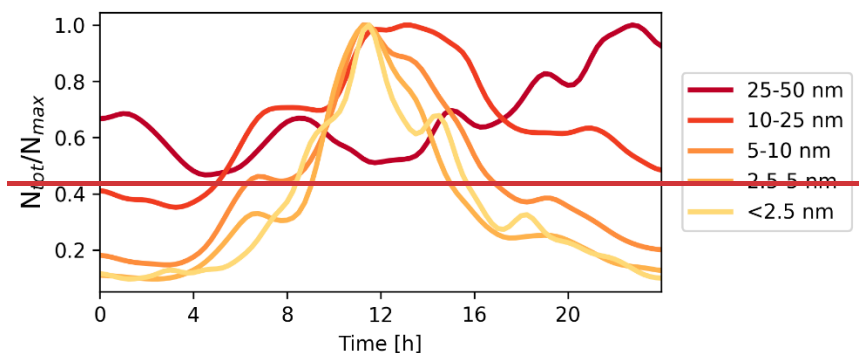


421

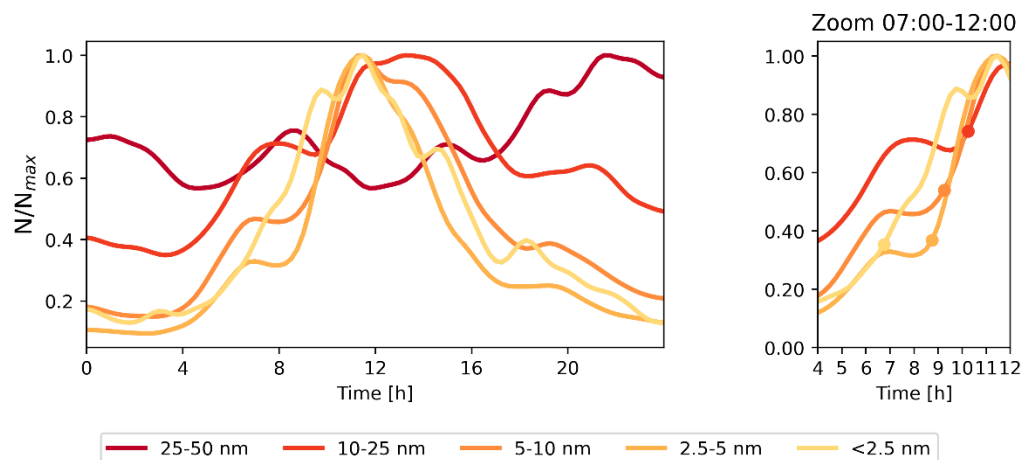
422 **Figure 6: Daily median particle number size distribution surface plots, grouped by into 20-percentile intervals of NPF rank (PR),**  
 423 **panels a-e). The bar plots indicate the number of equivalent days used to calculate the medians. For the definition of equivalent days,**  
 424 **see Fig. 5. Times are in Central European Time, UTC+1. Panel f shows the median size distributions for days with NPF rank below**  
 425 **the 20<sup>th</sup> percentile and above the 80<sup>th</sup> percentile. Median size distributions < 20 percentile of NPF rank days and > 80 percentile of**  
 426 **NPF rank days (panel f).**

427

428 Our analysis demonstrates that NPF significantly contributed to the UFP number concentration through a growth process that  
 429 lasted for several hours. As shown in Fig. 7, the concentration of sub-2.5 nm particles increased first, followed sequentially by  
 430 that of 2.5-5 nm, 5-10 nm, and 10-25 nm particles, reflecting a well-defined growth pattern in increasing size order. Accurately  
 431 distinguishing the contribution of NPF from that of primary emissions is crucial for a proper interpretation of these patterns.



432



433

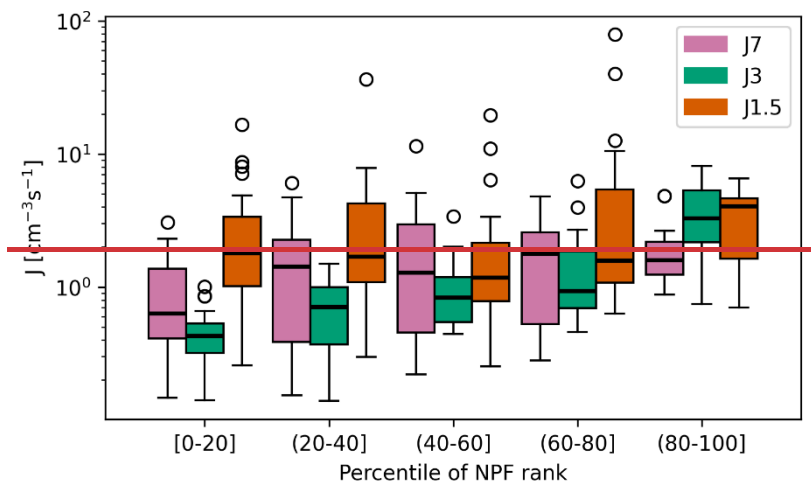
434 **Figure 7: a)** The lines represent the median total concentration of particles **within-in** different size bins (<2.5, 2.5-5, 5-10, 10-25, 25-  
 435 50 nm), calculated including the days above the 80<sup>th</sup> percentile of **NPF** rank. Each line is normalized to its own maximum value and  
 436 smoothed through a **one-dimensional Gaussian filter**, with a standard deviation of  $\sigma = 2$  samples; **b) zoom of the time interval between**  
 437 **7 and 12. The dots represent the first point where the derivative of the curve was larger than 0.03 and they mark the beginning of**  
 438 **the growth for each curve. The value 0.03 was chosen empirically.**

439 GR were calculated as described in Sect. 2.4.4. The values of  $1.8 \text{ nm h}^{-1}$ ,  $2.9 \text{ nm h}^{-1}$ , and  $9.7 \text{ nm h}^{-1}$  were found for the GR in  
 440 the size ranges of 3-7 nm, 7-20 nm, and 20-100 nm, respectively.

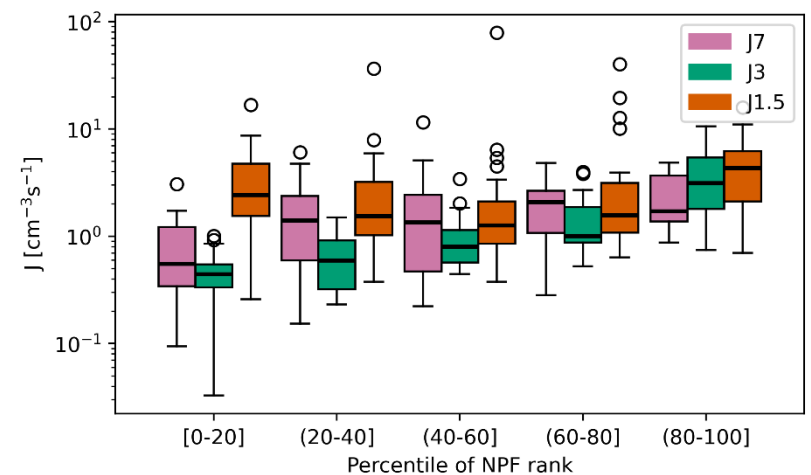
441 The formation rates  $J_{1.5}$ ,  $J_3$ , and  $J_7$  are presented in Fig. 8. While  $J_3$  correlated with percentile ranks - indicating higher  
 442 production of 3 nm particles (higher  $J_3$ ) during stronger NPF days (higher **ranking percentile rank**) -  $J_{1.5}$  remained relatively  
 443 constant across most ranks. This suggests that clustering, which formed 1.5 nm particles, occurred at the site, but only under  
 444 certain conditions the particle growth was observed (Kulmala et al., 2013).  $J_{1.5}$  reached higher values only in the 80-100 rank  
 445 bin, suggesting that clustering was more efficient during strong NPF days. Lastly,  $J_7$  did not show a clear increasing trend and  
 446 was often higher than  $J_3$ , likely due to the influence of traffic in this size range. This is supported by Fig. 4a5a, where morning  
 447 traffic peaks are clearly visible in the 5-10 nm size range. The ratio between  $J_7$  and  $J_3$  suggests that, for days with rank below  
 448 the 80<sup>th</sup> percentile, traffic was a stronger source of particles larger than 7 nm than NPF. During high-rank days (80<sup>th</sup> -100<sup>th</sup>  
 449 percentile), when NPF events were stronger, a marked increase in  $J_7$  would have been expected as result of a dominant

450 contribution from NPF. However, such an increase was not clearly observed, implying that traffic may have remained the  
 451 dominant contributor to particles larger than 7 nm even during the most intense NPF days. This result agrees with the discussion  
 452 in Sect. 3.1 about the relevant role of traffic compared to photochemistry in Milan in the 10-25 nm size range. As mentioned  
 453 in Sect. 2.4.4, formation rates were calculated only for the days when all the instruments were measuring simultaneously and,  
 454 therefore, the data availability shown in Fig. 2 should be taken into account when interpreting Fig. 8.

455



456

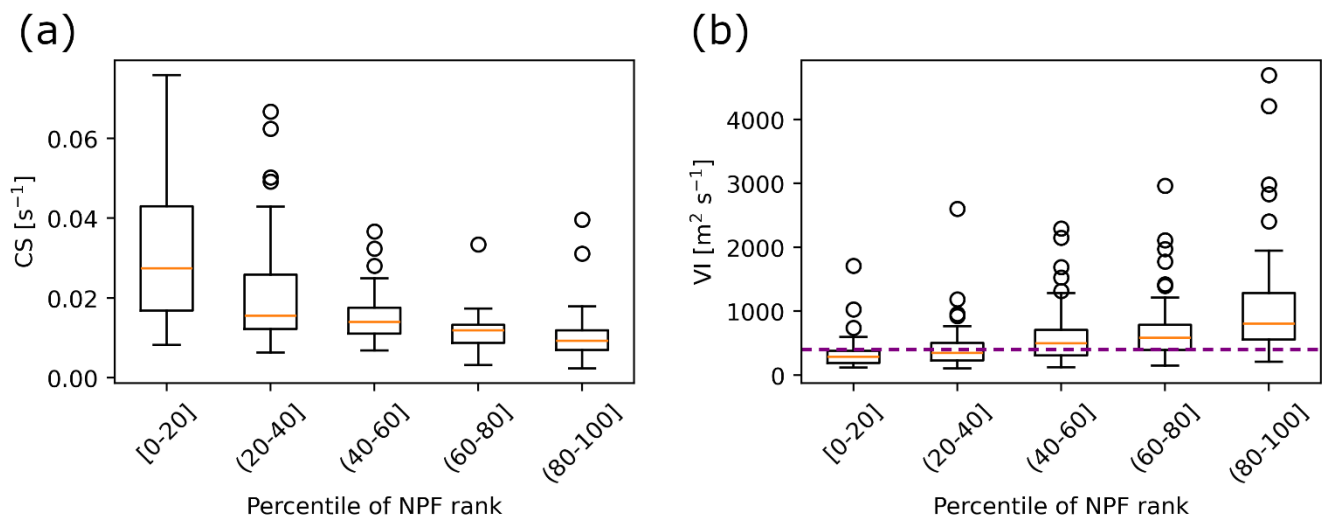
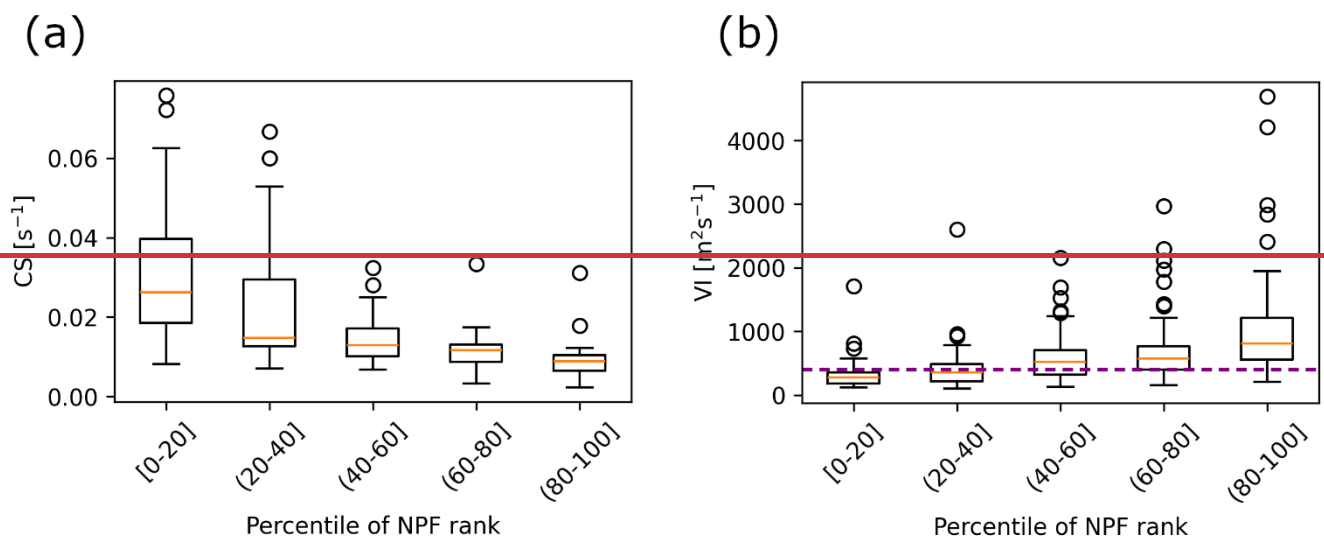


457

458 **Figure 8: Maximum  $J_{1.5}$ ,  $J_3$ , and  $J_7$  during the active window, per rank class. For the box-plot description, refer to Fig. 4**5b**.**

459 The Nano-particle ranking method allows a continuous analysis of the NPF process in relation to meteorological and dispersion  
 460 variables and pollutant concentrations. To understand which parameters affected the process, the atmospheric conditions within  
 461 each bin of 20-percentile of NPF rank were compared. Figure 9 illustrates the relationships of-between CS and ventilation  
 462 index VI, defined in Eq. (1), with-and rank as an example. Higher CS corresponded to low-rank days, while a high VI

463 corresponded to high-rank days. ~~Black carbon~~, NO<sub>2</sub>, ~~NO<sub>x</sub>, eBC~~, SO<sub>2</sub>, PM<sub>10</sub>, and PM<sub>2.5</sub> concentrations reported the same trend  
 464 as CS, while BLH behaved as the ventilation index (Fig. S54, S55, and S67). Therefore, enhanced NPF was, on average,  
 465 associated with cleaner air conditions and stronger atmospheric mixing. In particular, intermediate-strong NPF (percentile rank  
 466 > 60%) happened mostly during non-stagnant days and when the CS was relatively low (< 0.007 s<sup>-1</sup> on average). Therefore, it  
 467 is clear that cleaner air conditions and stronger atmospheric mixing correlated with enhanced NPF. In particular, intermediate-  
 468 strong NPF (percentile rank > 60%) happened, on average, only during non-stagnant days and low CS (< 0.007 s<sup>-1</sup> on average).  
 469 As reported in Sect. 2.4.3, the CS was calculated only for the days when both the SMPS and NAIS provided good data  
 470 availability. As a result, the CS time series contains several gaps (Fig. 2), which affect Fig. 9a.



473 **Figure 9: a) Median CS calculated over the active time window of each day and b) daily ventilation index (VI) per rank class. The**  
474 **purple dotted line represents the threshold of  $VI=400 \text{ m}^2\text{s}^{-1}$  for stagnant days. For the explanation of [the box-plots](#), refer to Fig. [45b](#).**

475 Our data allowed a comparison between the environmental conditions and NPF in Milan and [in](#) other urban locations. In Milan,  
476 the CS varied between  $0.01 \text{ s}^{-1}$  (during strong NPF events, Fig. 9a) and  $0.03 \text{ s}^{-1}$  (during weak NPF events, Fig. 9a), which is  
477 comparable to the values observed in Shanghai (CS between  $0.01 \text{ s}^{-1}$  and  $0.02 \text{ s}^{-1}$  on average; Yao et al., 2018). However, while  
478 the particle formation rate at  $1.5 \text{ nm}$  ( $J_{1.5}$ ) in Milan remained below  $10^2 \text{ cm}^{-3}\text{s}^{-1}$  (averaging around  $10^1 \text{ cm}^{-3}\text{s}^{-1}$ ), it reached up to  
479  $10^3 \text{ cm}^{-3}\text{s}^{-1}$  in Shanghai (Yao et al., 2018). This is likely due to differences in the precursor vapor concentrations and  
480 atmospheric conditions. However, without precursor vapor measurements in Milan, this hypothesis remains uncertain.

481 GR also differed between the two cities. In Shanghai, the GR was approximately  $6 \text{ nm h}^{-1}$  for 3-7 nm particles and  $9 \text{ nm h}^{-1}$   
482 for 7-25 nm particles (Yao et al., 2018), whereas in Milan, the values were significantly lower, specifically,  $1.8 \text{ nm h}^{-1}$  and  $2.9$   
483  $\text{nm h}^{-1}$  for 3-7 ~~nm~~ and 7-20 nm particles, respectively. A similar relation ~~is~~ was observed in Nanjing, where both recorded GR  
484 and J were higher than in Milan. For example, the average  $J_3$  in Nanjing ranged between  $7.4 \text{ cm}^{-3}\text{s}^{-1}$  and  $13.9 \text{ cm}^{-3}\text{s}^{-1}$ , while the  
485 GR of 10 nm particles was between  $13.4 \text{ nm h}^{-1}$  and  $14.5 \text{ nm h}^{-1}$ , depending on the type of event (Dai et al., 2023).

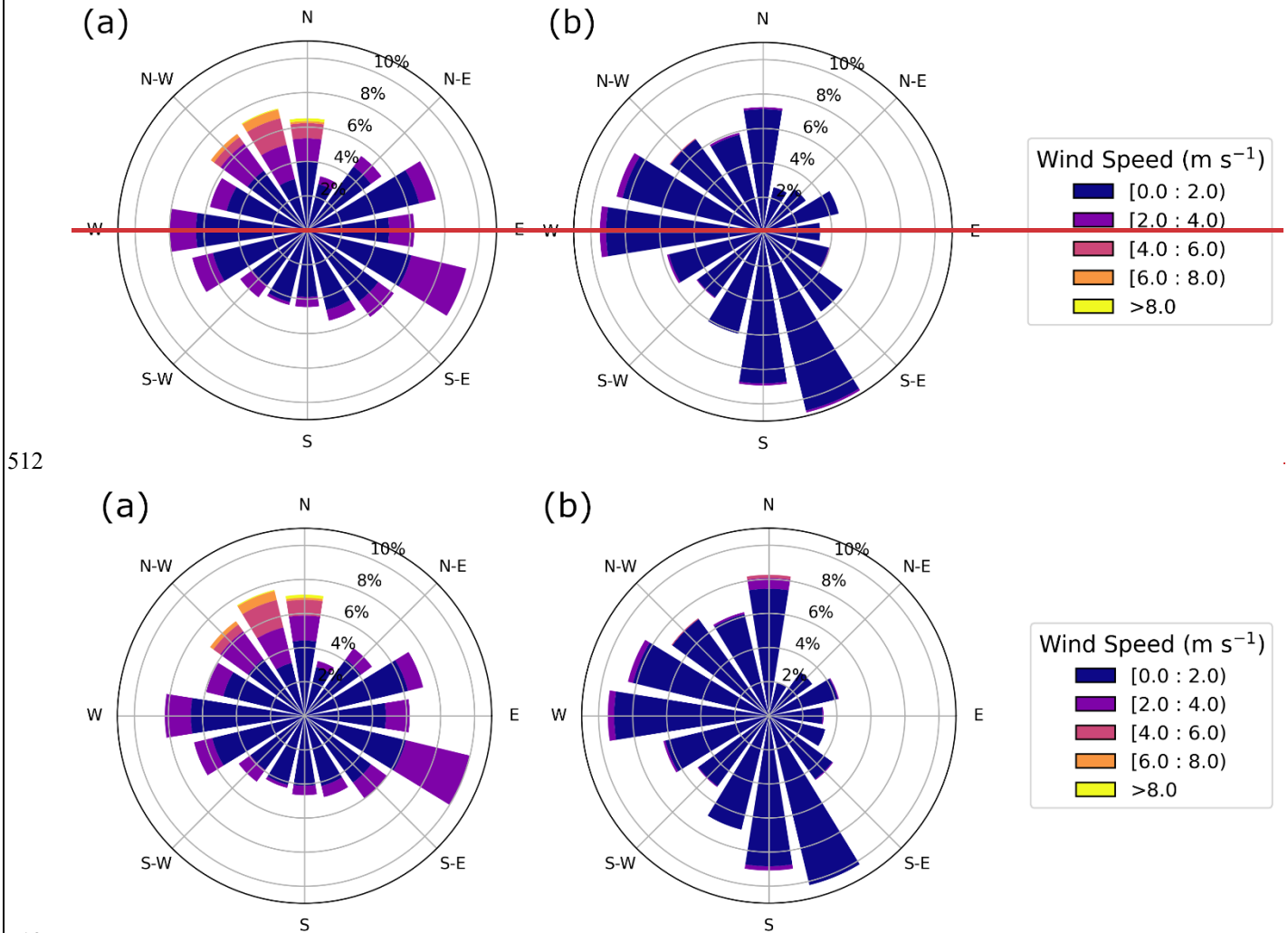
486 NPF has also been extensively studied in European cities. In Barcelona, for instance, Brean et al. (2020) reported an average  
487 GR of  $4.69 \text{ nm h}^{-1}$  and  $4.36 \text{ nm h}^{-1}$  for 4.5 and 1.9 nm particles, respectively. The CS in Barcelona was lower during NPF event  
488 days compared to non-event days, but it remained below  $0.02 \text{ s}^{-1}$  in both cases, slightly lower than the values recorded in Milan.  
489 When comparing formation rates, Milan exhibited weaker NPF. While  $J_{1.9}$  in Barcelona frequently fell between  $10 \text{ cm}^{-3}\text{s}^{-1}$  and  
490  $10^3 \text{ cm}^{-3}\text{s}^{-1}$  (Brean et al., 2020),  $J_{1.5}$  in Milan was mostly limited to the range of  $1 \text{ cm}^{-3}\text{s}^{-1}$  to  $10 \text{ cm}^{-3}\text{s}^{-1}$ , indicating a lower  
491 particle formation intensity. In Budapest, the GR of 6 nm particles was  $7.7 \text{ nm h}^{-1}$  on average, while  $J_6$  was  $4.2 \text{ cm}^{-3}\text{s}^{-1}$ , higher  
492 than what was observed in Milan in both cases. The CS in Budapest was lower than in Milan during non-event days but in line  
493 with Milan values during NPF event days (Salma et al., 2011). Finally, the study by Bousiotis et al. (2021) compared size  
494 distributions and NPF characteristics in several urban sites across Europe (Denmark, Germany, Spain, Finland, and Greece),  
495 distinguishing urban background and roadside sites. Reported  $J_{10}$  were higher in roadside sites, but overall lower than what  
496 was observed in Milan. On average, they remained below  $0.1 \text{ cm}^{-3}\text{s}^{-1}$  in all sites, except for German roadside sites, where the  
497 average  $J_{10}$  was higher but still below  $0.2 \text{ cm}^{-3}\text{s}^{-1}$ . The reasons for these differences may partially reside in the differences  
498 across sites, but they are not clear. GR for 10 nm particles was, on average, between  $2 \text{ nm h}^{-1}$  and  $5 \text{ nm h}^{-1}$ , in line with the  
499 value found in Milan for that of 7 nm particles ( $2.9 \text{ nm h}^{-1}$ ).

500 If we compare our results to previous studies in the rural areas of the Po Valley, it is clear that lower  $J_{1.5}$  were observed in  
501 Milan. Cai et al. (2024) observed an average  $J_{1.7}$  of  $10^2 \text{ cm}^{-3}\text{s}^{-1}$  in San Pietro Capofiume during NPF days, which was  
502 significantly higher than what was found in Milano ( $J_{1.5}$  was about  $3 \text{ cm}^{-3}\text{s}^{-1}$ ). However, the values for  $J_3$  and  $J_7$  were more  
503 similar. GR were also higher than in Milan (around  $4 \text{ nm h}^{-1}$  for 3-7 nm particles and around  $5 \text{ nm h}^{-1}$  for 7-15 nm particles).  
504 The recorded CS was below  $0.01 \text{ s}^{-1}$  during both NPF and non-NPF and therefore lower than in Milan, where NPF is possibly  
505 more suppressed ~~more~~ than in the rural areas.

506 When comparing all the results, though, it is critical to take into consideration the possible differences in the methodologies  
507 for estimating the formation and growth rates, including the slightly different size ranges used in different studies, which  
508 contribute to the uncertainty in of the comparisons.

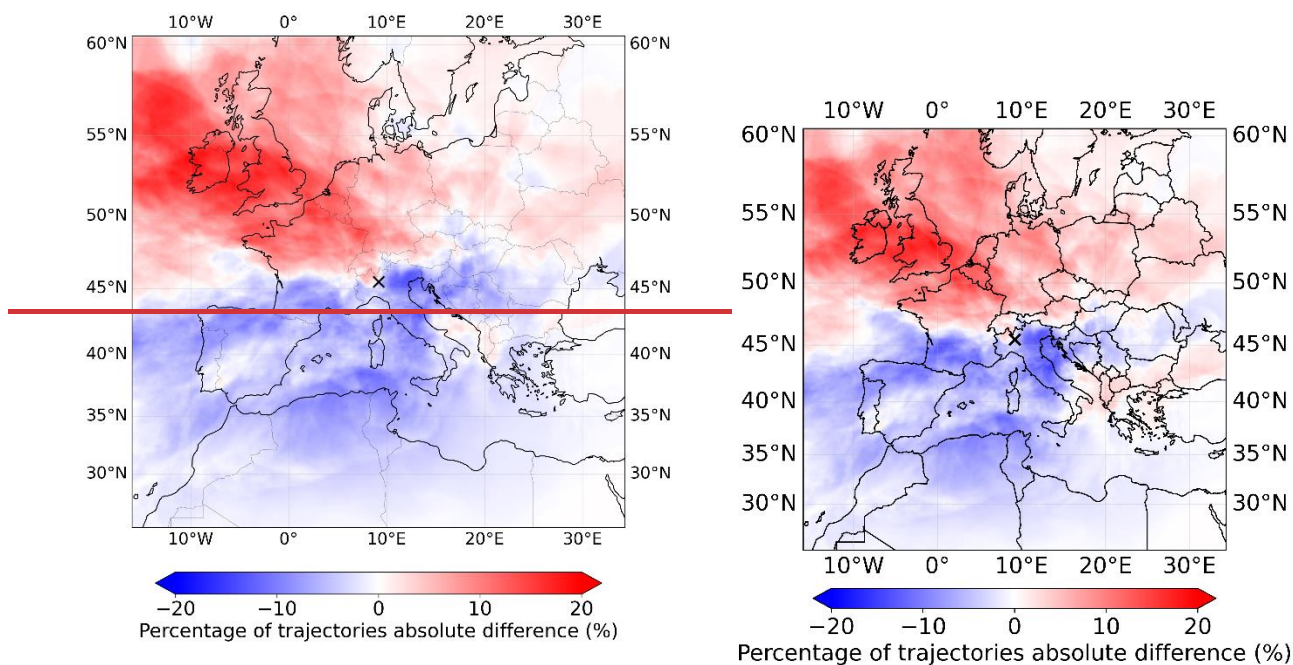
### 509 3.3 Air mass modelling-analysis in relation to NPF

510 The analysis of NPF in relation to the meteorological conditions at the site pointed out that strong wind from northwest was a  
511 favorable condition for NPF at this site (Fig. 10).



513  
514 **Figure 10: Wind rose for a) strong NPF days (percentile rank > 80) and for b) weak NPF days (percentile rank < 20).**

515 In order to explore further such relation and the characteristics of the air masses that favor the formation of new particles, the  
516 Lagrangian particle dispersion model FLEXPART, driven by the meteorological output from WRF simulations, was applied  
517 to identify the eventual preferential air mass direction for NPF and its characteristics.



518

519

520 **Figure 11: Air masses reaching the measurement site. The color scale represents the difference between the percentage of trajectories**  
521 **passing over a given area and reaching Milan during a day with a percentile rank > 80 and the percentage of the total trajectories**  
522 **passing over a given area. The details of the metric are reported in Sect. 2.4.7. An X marks the location of Milan on the map.**

523 The air mass trajectory density, calculated as described in Eq. (8), emphasizes that north, particularly northwest, was the  
524 preferred direction for NPF (Fig. 11). An east-west axis distinctly separated the north and south sectors: air masses arriving in  
525 Milan from the north promoted NPF, while those from the south hindered it.

526 Focusing on the Po Valley only (Fig. 12), it is clear that a lower air mass residence time in the area produced stronger NPF.

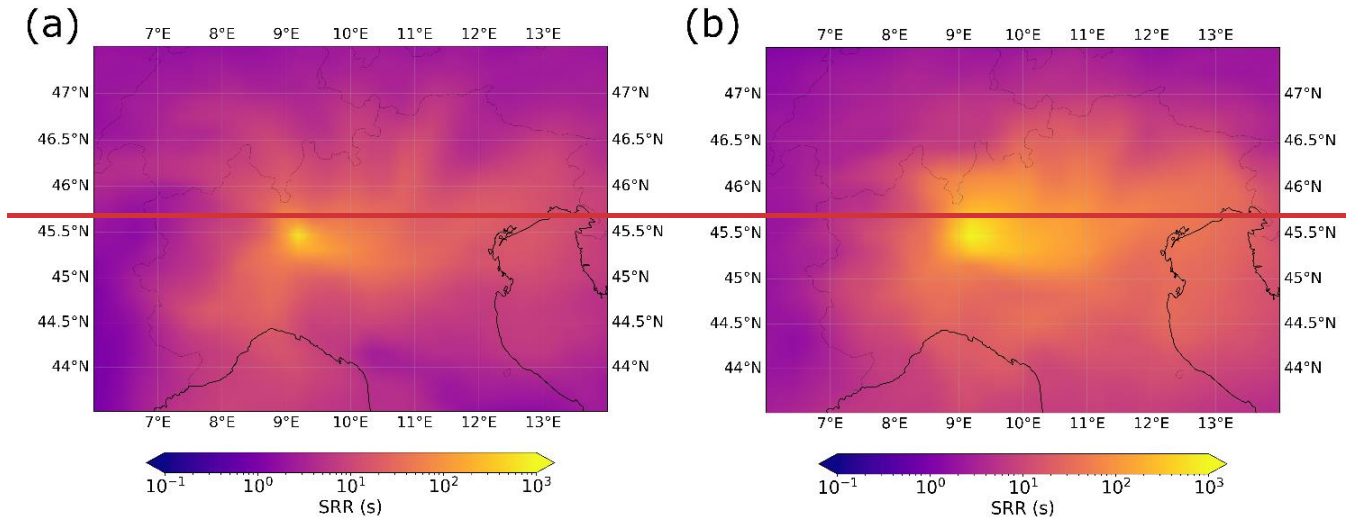
527 This agrees with both the anticorrelation between NPF rank and wind speed and with the anticorrelation between NPF rank

528 and pollutant concentrations, as the Po Valley is rich in emission sources. Lower exposure to anthropogenic sources-emissions  
529 enhanced NPF in this location, as shown in Fig. 13. Lower air mass exposure to NO<sub>x</sub> and SO<sub>2</sub> sources-emissions was associated

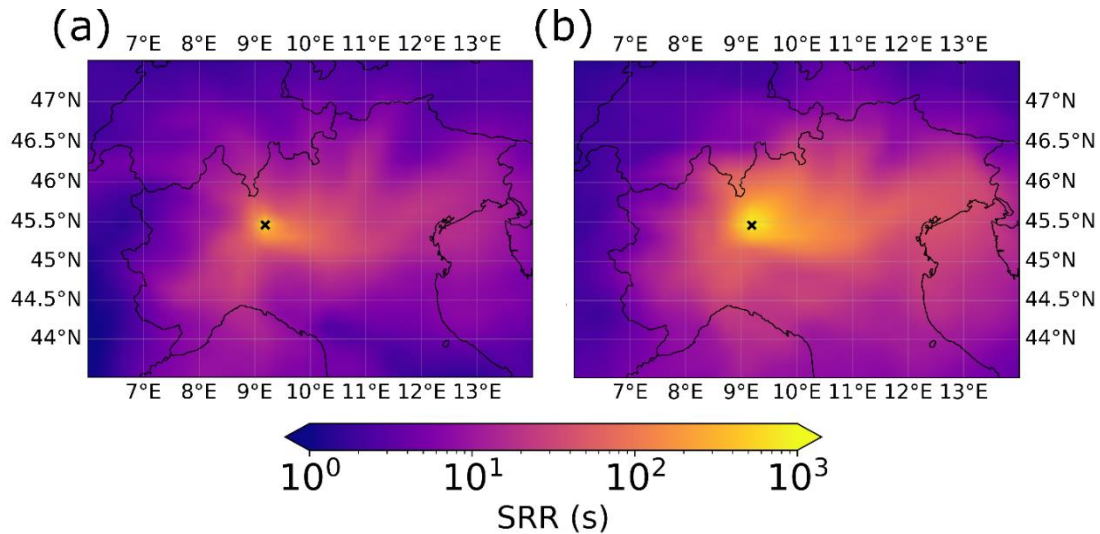
530 with higher concentration of small (sub-2.5 nm) particles, to a broader cluster band, extending to 2.5 nm, and to a smaller  
531 accumulation mode. On the other hand, at higher NO<sub>x</sub> and SO<sub>2</sub> air mass exposure, the cluster particles remained smaller (up

532 to ~1.5 nm) and had lower concentrations. Furthermore, the accumulation mode reached larger sizes. Overall, these  
533 observations indicate that lower air mass exposure to anthropogenic sources-emissions favored the formation of new particles.

534 The air mass exposure to both NO<sub>x</sub> and SO<sub>2</sub> ~~sources-emissions anti~~correlated with the median ventilation index, which  
 535 decreased at increasing air mass exposure, supporting the role of atmospheric ventilation (Fig. 13). Considering the data  
 536 availability described in Fig. 2, the number of data points used in the calculation of the average concentrations shown in Fig.  
 537 13 may vary depending on the diameter.

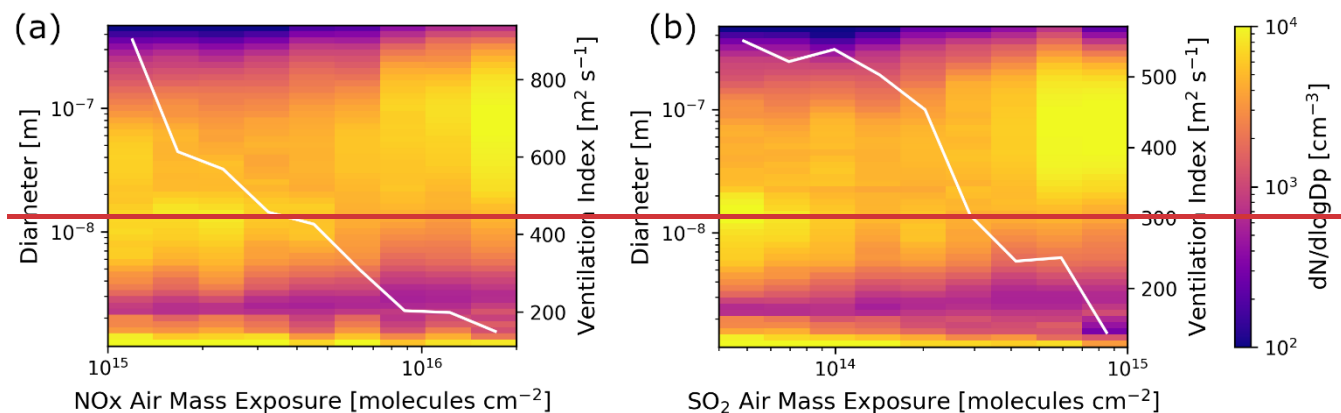


538



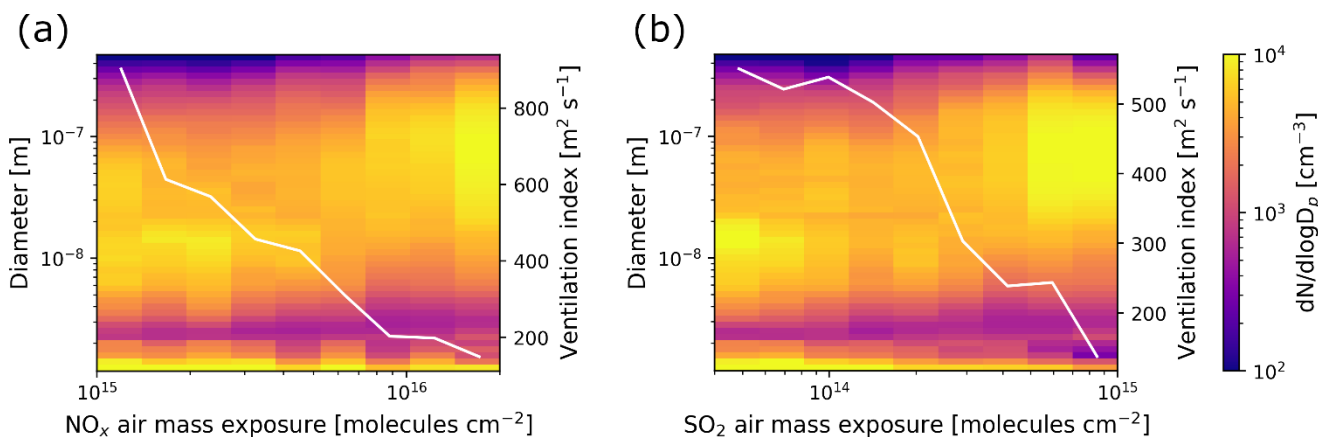
539

540 **Figure 12: Source-Receptor Relationship (SRR) below 500 m during a) strong NPF days (percentile rank > 80) and during b) weak**  
 541 **NPF days (percentile rank < 20). The x marks indicate the study site.**



542

543



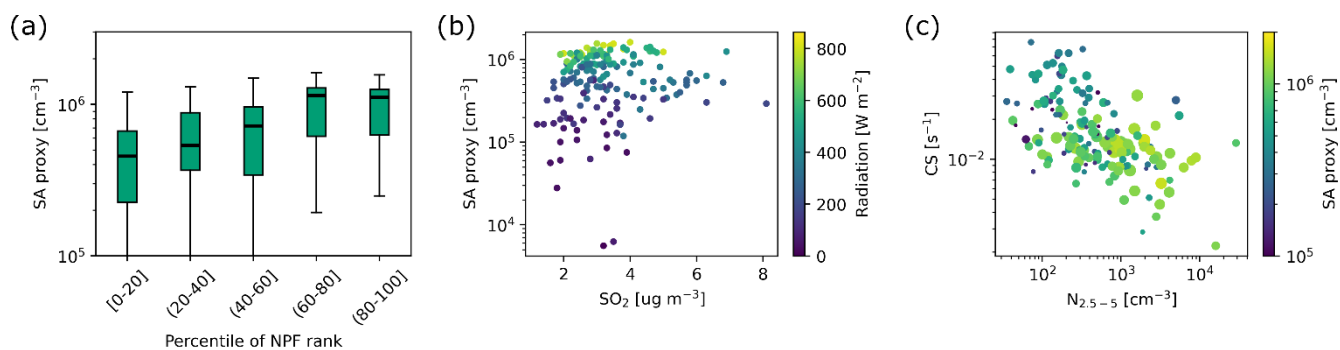
544

545 **Figure 13: Relationship between a) Air mMass eExposure to NO<sub>x</sub> emissions and particle number size distribution and b) aAir**  
 546 **mMass eExposure to SO<sub>2</sub> emissions and particle number size distribution. The white lines represent the median V<sub>v</sub>entilation I<sub>I</sub>ndex.**

### 547 3.4 Sulfuric acid proxy analysis

548 The role of sulfuric acid, which has been identified in previous studies as a critical precursor vapor in the Po Valley (Cai et al.,  
 549 2024), was investigated through its proxy, calculated as described in Sect. 2.4.5. The sulfuric acid proxy showed an increasing  
 550 trend with percentile ranks (Fig. 14b), indicating its contribution to the NPF process. However, SO<sub>2</sub>, a precursor for sulfuric  
 551 acid, showed the opposite trend (Fig. 14a), similar to that of CS and of other pollutants (BC, PM<sub>10</sub>, PM<sub>2.5</sub>, NO<sub>2</sub>). This hints at  
 552 the role of high CS in inhibiting NPF.

553 The role of sulfuric acid, which has been identified in previous studies as a critical precursor vapor in the Po Valley (Cai et al.,  
 554 2024), was investigated through its proxy, calculated as described in Sect. 2.4.5. The sulfuric acid proxy exhibited an increasing  
 555 trend with the percentile of NPF rank (Fig. 14a), suggesting its potential contribution to the NPF process.

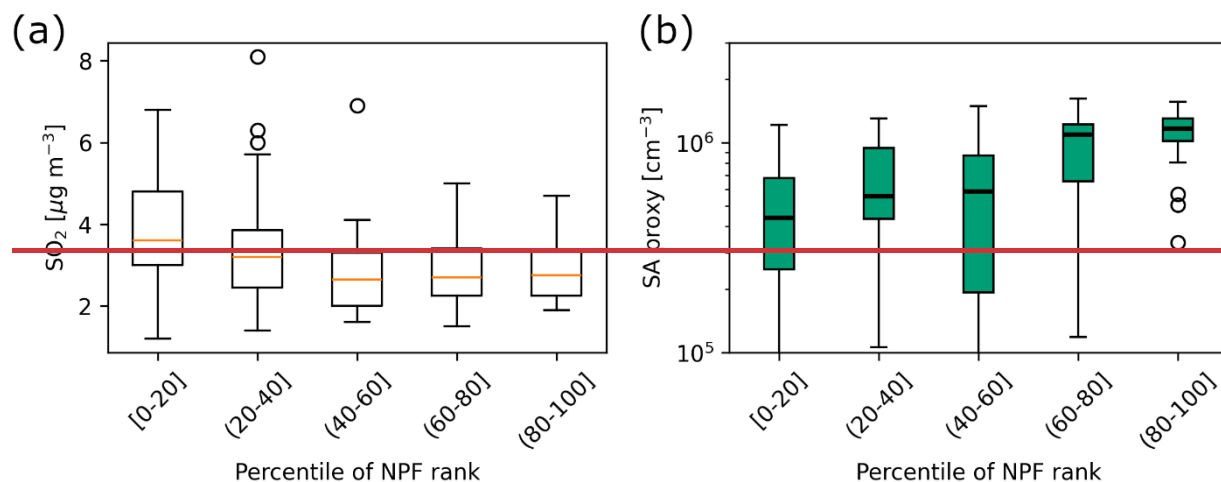


556

557 **Figure 14: a) Sulfuric acid (SA) proxy daily median calculated over the active time window per rank class. For the description of**  
 558 **the boxplots, refer to Fig. 4b; b) relation between sulfuric acid (SA) proxy, SO<sub>2</sub> concentration, and radiation; c) relation between**  
 559 **CS, sulfuric acid (SA) proxy, and N<sub>2.5-5</sub>, representing NPF intensity as explained in Sect. 2.4.1. The size of the dots represents the**  
 560 **radiation. For both panels b and c, each point is the daily median calculated over the active time window.**

561 No clear correlation between sulfuric acid and SO<sub>2</sub> concentrations was observed (Fig. 14b), indicating that SO<sub>2</sub> was not a  
 562 limiting factor for sulfuric acid formation in Milan. On the other hand, sulfuric acid showed a clear increase with radiation  
 563 (Fig. 14b and more clearly, Fig. S8), hinting at the role of photochemical processes for its formation rather than SO<sub>2</sub> availability  
 564 or a sink effect. Indeed, while on average, a higher sulfuric acid proxy was recorded in correspondence with lower CS (Fig.  
 565 S8), several cases with low CS and low sulfuric acid were observed and were linked to low radiation.

566 The relative roles of CS and sulfuric acid in NPF were then investigated using the concentration of 2.5-5 nm particles as a  
 567 proxy for NPF intensity (Sect. 2.4.1). Figure 14c clearly presents an inverse correlation between N<sub>2.5-5</sub> and CS, indicating the  
 568 relevant role of the CS in enhancing the NPF mechanism. On average, higher concentrations of sulfuric acid proxy were  
 569 associated with stronger NPF (Fig. 14a and Fig. 14c). However, given the large variability in the trend, its role is less clear.  
 570 The gaps in the CS time series due to the limited SMPS data coverage are reflected into the SA proxy time series and may  
 571 affect Fig. 14.



572

573 ~~Figure 14: a) SO<sub>2</sub> daily median concentration calculated over the active time window and b) sulfuric acid (SA) proxy daily median~~  
574 ~~calculated over the active time window per rank class. For the description of the box plots, refer to Fig. 5b.~~

### 575 3.5 NPF drivers in different atmospheric regimes

576 The results described so far were obtained using the entire dataset regardless of the environmental conditions. However,  
577 treating different atmospheric regimes, such as ventilated and stagnant conditions or different seasons together may create  
578 biases in the interpretation of the drivers of NPF and hide potentially relevant patterns.

579 To evaluate the robustness of our conclusions in different regimes, we performed an additional stratified analysis separating  
580 stagnant and non-stagnant conditions and different seasons (see Supplementary Materials) and applying the nano-particle  
581 ranking analysis on each subset. The two analyses (seasons and stagnant/non-stagnant) were performed separately, and the  
582 stratifications were not combined due to the limited amount of data.

583 Despite the differences in background conditions, the main conclusions did not change when analyzing separately stagnant  
584 and non-stagnant periods. CS values were generally higher under stagnant conditions compared to non-stagnant ones; however,  
585 in both regimes, the CS decreased with increasing NPF rank, indicating that stronger NPF preferentially occurred under lower  
586 CS conditions, independently of the level of stagnation (Fig. S9a). SO<sub>2</sub> concentrations showed a less clear behavior and did  
587 not appear to limit NPF both under stagnant and non-stagnant conditions (Fig. S9b). Sulfuric acid proxy and J<sub>3</sub> increased with  
588 NPF rank in both regimes (Fig. S9c, Fig. S9d).

589 Considering that seasonality may have still introduced some bias in the interpretation of these results (Table S1), a separate  
590 study for each season was performed.

591 Seasonal stratification revealed higher CS values in winter compared to the other seasons. In winter and autumn, the CS clearly  
592 decreased with increasing NPF rank, while this relation was weaker in spring and summer (Fig. S11a). J<sub>3</sub> was more difficult  
593 to interpret on a seasonal basis, particularly in summer, due to the limited data availability. Nevertheless, J<sub>3</sub> generally increased  
594 with NPF rank in all seasons, consistently with the results from the non-stratified dataset (Fig. S11e).

595 SO<sub>2</sub> concentrations were generally higher in winter than in the other seasons due to the enhanced emissions and the weaker  
596 dispersion conditions. In winter, SO<sub>2</sub> showed a decreasing trend with increasing NPF rank (Fig. S11c), in agreement with the  
597 opposite relation between NPF rank and SO<sub>2</sub> observed in the non-stratified analysis. In spring, summer, and autumn, SO<sub>2</sub>  
598 concentrations were lower and did not exhibit a clear trend with NPF rank. Similar SO<sub>2</sub> levels associated with both weak and  
599 strong NPF events suggest that SO<sub>2</sub> availability was not a limiting factor for NPF intensity during these seasons. The sulfuric  
600 acid proxy did not show a clear relation with NPF rank in most seasons, except for autumn, when an increasing trend was  
601 observed (Fig. S11d).

602 The analysis of NPF after stratifying different atmospheric conditions does not contradict the results obtained with the entire  
603 dataset. However, drawing conclusions may be misleading. In fact, the stratification led to a low amount of data per class,  
604 reducing the reliability of the results. Furthermore, the NPF intensities in the different groups (seasons, stagnant and non-  
605 stagnant) may not be comparable, considering that the nano-particle ranking was applied separately on each subset (Fig. S10).

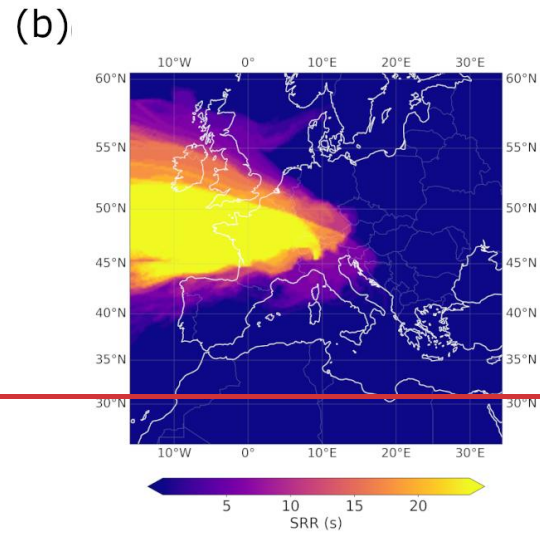
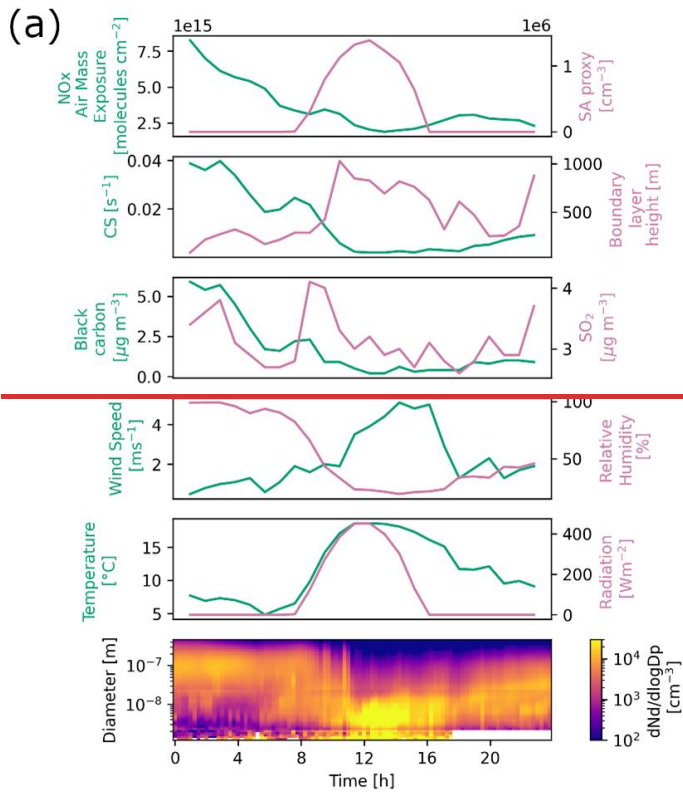
606 To assess this, the concentration of 2.5-5 nm particles was also used as proxy for NPF intensity other than the percentile rank  
607 (Fig. S11f, Fig. S11g).  
608 A larger dataset would allow a more in-depth analysis of how different regimes may affect NPF and of the main drivers of this  
609 process in various atmospheric conditions.

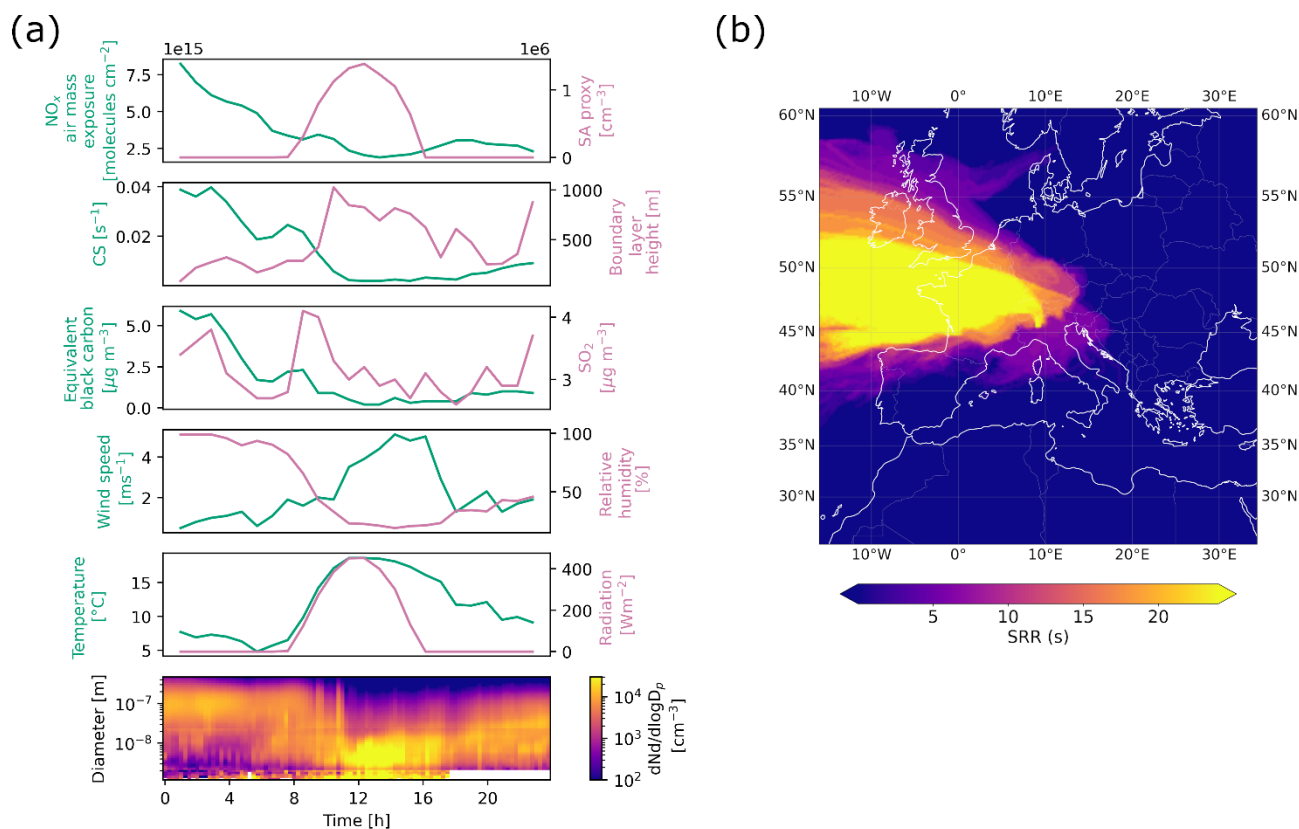
### 610 **3.65 Case study**

611 In this section, we present an example of NPF day, featuring the characteristics discussed so far (lower CS and eBC  
612 concentration, higher BLH, and lower exposure to anthropogenic emissions). Specifically, we focus on November 17<sup>th</sup>, 2023,  
613 a day that fell within the 80-100 class of percentile rank (Fig. 15). On this day, local clustering led to an increase in the  
614 concentration of sub-3 nm particles starting at 8 am (UTC+1), followed by a subsequent rise in the concentration of particles  
615 up to 100 nm in diameter (Fig. 15a), indicating condensational growth. These phenomena were observed in correspondence  
616 with a decrease in CS, in eBC concentration, and in air mass exposure to NO<sub>x</sub> sources emissions, as well as an increase in wind  
617 speed and BLH (Fig. 15a), suggesting strong atmospheric mixing. Additionally, the air mass trajectory analysis revealed a  
618 dominant flow from northwest (Fig. 15b). Oppositely to the average results, ~~that have been shown so far,~~ SO<sub>2</sub> concentration  
619 showed a sharp increase as the event began.

620 On this day, the phenomenon driving the free tropospheric air masses advection and atmospheric clearing was the Foehn wind,  
621 ~~a~~ a warm, dry wind descending from the Alps, ~~—~~ which brings clear skies and higher temperatures compared to seasonal  
622 averages, together with exceptionally low pollutant concentrations in the Po Valley. Specifically, on November 17<sup>th</sup>, 2023, the  
623 Foehn wind was identified by the decrease in relative humidity, the daytime median temperature of 17.2°C (above the daily  
624 monthly average of 11.8°C), and the smooth radiation trend, indicating the absence of cloud cover. The air mass trajectory  
625 also confirmed the presence of this wind pattern. The increase in SO<sub>2</sub>, the source of which still needs to be confirmed, may  
626 have further enhanced the formation of new particles, together with the decrease in CS.

627 Similar cases have been observed during the campaign but a detailed classification of Foehn wind event days would be needed  
628 to further characterize them in relation to NPF. This case study is consistent with the earlier observations that Foehn wind can  
629 create favorable conditions ~~to~~ for NPF in the Po Valley (Rodríguez et al., 2005) and that it is a significant source of UFP even  
630 in urban Milan.





632

633 **Figure 15: a) NO<sub>x</sub> air mass exposure, sulfuric acid (SA) concentration proxy, CS, BLH, eBC and SO<sub>2</sub> concentrations, wind speed,**  
 634 **relative humidity, temperature, and radiation time series and particle number size distribution surface plot during November 17<sup>th</sup>,**  
 635 **2023; b) Source-Receptor Relationship (SRR) for all the trajectories arriving during November 17<sup>th</sup>, 2023.**

## 636 4 Conclusions

637 This study examines NPF in Milan over one year, revealing that NPF was more intense during spring and summer, resulting  
 638 in higher concentrations of sub-10 nm particles. In contrast, winter saw higher levels of particles larger than 50 nm, mostly  
 639 due to the reduced BLH and increased emissions from heating sources. Traffic-related peaks during rush hours were more  
 640 evident in winter and autumn, but they diminished in spring and summer as atmospheric mixing increased. Our analysis shows  
 641 that cleaner, well-mixed conditions, particularly with strong northwesterly winds, enhanced NPF by reducing the CS, possibly  
 642 allowing precursor vapors to participate in the formation of new particles. Reduced air mass exposure to anthropogenic **sources**  
 643 **emissions** and shorter residence time in the Po Valley further supported stronger NPF.

644 The driving mechanisms of NPF vary by location and environmental conditions. Similar patterns have been observed in other  
 645 urban areas, such as Beijing, China, where Guo et al. (2014) found a higher frequency of NPF events during cleaner periods  
 646 characterized by lower particle **number** concentrations. During these periods, the reduced CS allowed nucleating vapors to  
 647 accumulate, facilitating NPF. Conversely, in polluted conditions with high aerosol loading, NPF was suppressed due to the

648 high CS and the abundant pre-existing particles, which provided surfaces that scavenge vapors, inhibiting the NPF process.  
649 Also, in Beijing, the occurrence of both clean and polluted periods depended on the meteorology as strong winds descending  
650 from the mountains in the north contributed to the cleaning of the atmosphere, while the slower winds from the south favored  
651 the accumulation of pollutants (Guo et al., 2014). Our findings suggest that a similar mechanism may be happening in Milan.  
652 While the absence of direct precursor vapor measurements precludes us from entirely dismissing the influence of transported  
653 chemical precursors, the geographical and environmental context of Milan supports a more plausible explanation. Located in  
654 a heavily industrialized, densely populated region with significant agricultural activities, it is reasonable to believe that the  
655 reduction of the CS played a more prominent role in initiating NPF, rather than an eventual influx of precursors from the Alps.  
656 The relationship between wind speed and NPF is not uniform across all urban sites. For instance, Pushpawela et al. (2019)  
657 explored this relationship in Brisbane, Australia, and observed that NPF was more likely to happen on days with lower wind  
658 speed, a finding opposite to that in Milan and other highly polluted environments. Their comparative analysis suggested that  
659 the impact of wind speed on NPF depends on the level of pollution and the distribution of precursor vapors. In relatively  
660 cleaner urban areas like Brisbane, where the accumulation of precursors can enhance NPF, a lower wind speed facilitates this  
661 process. In contrast, in highly polluted cities like Beijing, a low wind speed increases the CS, suppressing NPF. At higher wind  
662 speed, the reduction in CS can promote NPF in polluted areas by clearing pre-existing particles, whereas in cleaner cities, the  
663 removal of precursor vapors can inhibit NPF. Our study locates Milan within this framework as a highly polluted city where  
664 the interplay between wind speed, CS, and precursor vapor concentrations played a critical role in the NPF dynamics.

665

666 The findings hint at potential implications for air quality in Milan. Long-term reductions in PM<sub>10</sub> and PM<sub>2.5</sub> concentrations,  
667 potentially driven by regulatory measures, could lead to stronger NPF, increasing the concentrations of UFP. This highlights  
668 the need for detailed studies on precursor vapors and on the chemical pathways leading to NPF to fully understand their role  
669 in the NPF process, especially in relation to low CS episodes. Future research should focus on the direct measurements of  
670 these precursors to clarify their contributions, whether local or transported. Comparative studies in other polluted urban  
671 environments are also crucial to understand regional differences in NPF dynamics. Long-term monitoring of aerosol  
672 concentrations at-in all size ranges and of NPF events, in relation to urban development and pollution control, would provide  
673 valuable insights into the effectiveness and results of air quality strategies.

#### 674 **Data availability**

675 The size distribution data from the nCNC, NAIS, and SMPS presented in this work are publicly available at  
676 <https://doi.org/10.5281/zenodo.18130252> (Agrò, 2026).

677 The raw data are available from the corresponding author (myriam.agro@helsinki.fi) upon request.

678 **Author contribution**

679 The study was designed by FB and TP. MA, SM, IG, PF, AB, CO, AB, JS participated in the installation and the operation of  
680 the instruments. MA analysed the data. MB and GC performed the modelling simulations and analysis. MA prepared the  
681 manuscript. All the coauthors contributed to the discussion and interpretation of the results and the revision of the article.

682 **Competing interests**

683 Some authors are members of the editorial board of journal Atmospheric Chemistry and Physics.

684 **Acknowledgments**

685 We acknowledge the use of the Matlab package psm-dataflow-tools by Lauri Ahonen for the [PSM-inversion of the nCNC data](#).  
686 We thank the Department of Direzione tecnica monitoraggio e prevenzione del rischio naturale of [the](#) Regional Agency for  
687 Environmental Protection of Lombardy for providing the boundary layer height data. Model simulations were performed on  
688 the Mahti supercomputer of the Finnish IT Center for Science (CSC).

689 **Financial support**

690 This project received funding from the European Union's Horizon 2020 research and innovation programme under grant  
691 agreement No 101036245 (RI-URBANS).  
692 We thank the ACCC Flagship, funded by the Academy of Finland grant numbers 337549 (UH) and 337552 (FMI).

693 **References**

- 694 [Agrò, M.: Data of "Ventilation and low pollution enhancing new particle formation in Milan, Italy", Zenodo,](#)  
695 <https://doi.org/10.5281/zenodo.18130252>, 2026.
- 696 Aliaga, D., Tuovinen, S., Zhang, T., Lampilahti, J., Li, X., Ahonen, L., Kokkonen, T., Nieminen, T., Hakala, S., Paasonen, P.,  
697 Bianchi, F., Worsnop, D., Kerminen, V.-M., and Kulmala, M.: Nanoparticle ranking analysis: determining new particle  
698 formation (NPF) event occurrence and intensity based on the concentration spectrum of formed (sub-5&thinsp;nm) particles,  
699 *Aerosol Res.*, 1, 81–92, <https://doi.org/10.5194/ar-1-81-2023>, 2023.
- 700 Bae, M.-S., Schwab, J. J., Hogrefe, O., Frank, B. P., Lala, G. G., and Demerjian, K. L.: Characteristics of size distributions at  
701 urban and rural locations in New York, *Atmospheric Chem. Phys.*, 10, 4521–4535, <https://doi.org/10.5194/acp-10-4521-2010>,  
702 2010.
- 703 Batchvarova, E. and Gryning, S.-E.: Applied model for the growth of the daytime mixed layer, *Bound.-Layer Meteorol.*, 56,  
704 261–274, <https://doi.org/10.1007/BF00120423>, 1991.

- 705 Bettineschi, M., Vitali, B., Cholakian, A., Zardi, D., Bianchi, F., Sinclair, V., Mikkola, J., Cristofanelli, P., Marinoni, A.,  
 706 Mazzini, M., Heikkinen, L., Aurela, M., Paglione, M., Bessagnet, B., Tuccella, P., and Ciarelli, G.: Across land, sea, and  
 707 mountains: sulphate aerosol sources and transport dynamics over the northern Apennines, *Environ. Sci. Atmospheres*, 5, 1023–  
 708 1034, <https://doi.org/10.1039/D5EA00035A>, 2025.
- 709 Bousiotis, D., Pope, F. D., Beddows, D. C. S., Dall’Osto, M., Massling, A., Nøjgaard, J. K., Nordstrøm, C., Niemi, J. V.,  
 710 Portin, H., Petäjä, T., Perez, N., Alastuey, A., Querol, X., Kouvarakis, G., Mihalopoulos, N., Vratolis, S., Eleftheriadis, K.,  
 711 Wiedensohler, A., Weinhold, K., Merkel, M., Tuch, T., and Harrison, R. M.: A phenomenology of new particle formation  
 712 (NPF) at 13 European sites, *Atmospheric Chem. Phys.*, 21, 11905–11925, <https://doi.org/10.5194/acp-21-11905-2021>, 2021.
- 713 Brean, J., Beddows, D. C. S., Shi, Z., Temime-Roussel, B., Marchand, N., Querol, X., Alastuey, A., Minguillón, M. C., and  
 714 Harrison, R. M.: Molecular insights into new particle formation in Barcelona, Spain, *Atmospheric Chem. Phys.*, 20, 10029–  
 715 10045, <https://doi.org/10.5194/acp-20-10029-2020>, 2020.
- 716 Brioude, J., Arnold, D., Stohl, A., Cassiani, M., Morton, D., Seibert, P., Angevine, W., Evan, S., Dingwell, A., Fast, J. D.,  
 717 Easter, R. C., Pisso, I., Burkhardt, J., and Wotawa, G.: The Lagrangian particle dispersion model FLEXPART-WRF version  
 718 3.1, *Geosci. Model Dev.*, 6, 1889–1904, <https://doi.org/10.5194/gmd-6-1889-2013>, 2013.
- 719 Cai, J., Sulo, J., Gu, Y., Holm, S., Cai, R., Thomas, S., Neuberger, A., Mattsson, F., Paglione, M., Decesari, S., Rinaldi, M.,  
 720 Yin, R., Aliaga, D., Huang, W., Li, Y., Gramlich, Y., Ciarelli, G., Quéléver, L., Sarnela, N., Lehtipalo, K., Zannoni, N., Wu,  
 721 C., Nie, W., Kangasluoma, J., Mohr, C., Kulmala, M., Zha, Q., Stolzenburg, D., and Bianchi, F.: Elucidating the mechanisms  
 722 of atmospheric new particle formation in the highly polluted Po Valley, Italy, *Atmospheric Chem. Phys.*, 24, 2423–2441,  
 723 <https://doi.org/10.5194/acp-24-2423-2024>, 2024.
- 724 Chen, F. and Dudhia, J.: Coupling an Advanced Land Surface–Hydrology Model with the Penn State–NCAR MM5 Modeling  
 725 System. Part I: Model Implementation and Sensitivity, 2001.
- 726 [Colombi, C., Cuccia, E., Dal Santo, U., Franciosa, M., Lanzani, G., Petrosino, F., Vincenzi, D., Bacco, D., Poluzzi, V., Scotto,](#)  
 727 [F., Trentini, A., Bardi, L., Bruno, A., De Maria, R., Sacco, M., Pistollato, S., Zagolin, L., Magri, T., and Diémoz, H.:](#)  
 728 [Monitoring the environmental effects of pollutant reduction measures implemented by air quality improvement plans – Report](#)  
 729 [on source apportionment, 2023.](#)
- 730 [Dal Maso, M., Kulmala, M., Riipinen, I., Wagner, R., Hussein, T., Aalto, P. P., and Lehtinen, K. E. J.: Formation and growth](#)  
 731 [of fresh atmospheric aerosols: eight years of aerosol size distribution data from SMEAR II, Hyytiälä, Finland, 2005.](#)
- 732 Dada, L., Ylivinkka, I., Baalbaki, R., Li, C., Guo, Y., Yan, C., Yao, L., Sarnela, N., Jokinen, T., Daellenbach, K. R., Yin, R.,  
 733 Deng, C., Chu, B., Nieminen, T., Wang, Y., Lin, Z., Thakur, R. C., Kontkanen, J., Stolzenburg, D., Sipilä, M., Hussein, T.,  
 734 Paasonen, P., Bianchi, F., Salma, I., Weidinger, T., Pikridas, M., Sciare, J., Jiang, J., Liu, Y., Petäjä, T., Kerminen, V.-M., and  
 735 Kulmala, M.: Sources and sinks driving sulfuric acid concentrations in contrasting environments: implications on proxy  
 736 calculations, *Atmospheric Chem. Phys.*, 20, 11747–11766, <https://doi.org/10.5194/acp-20-11747-2020>, 2020.
- 737 Dada, L., Okuljar, M., Shen, J., Olin, M., Wu, Y., Heimsch, L., Herlin, I., Kankaanrinta, S., Lampimäki, M., Kalliokoski, J.,  
 738 Baalbaki, R., Lohila, A., Petäjä, T., ~~Dal~~ Maso, M.-D., Duplissy, J., Kerminen, V.-M., and Kulmala, M.: The synergistic role  
 739 of sulfuric acid, ammonia and organics in particle formation over an agricultural land, *Environ. Sci. Atmospheres*, 3, 1195–  
 740 1211, <https://doi.org/10.1039/D3EA00065F>, 2023.
- 741 Dai, L., Zhao, Y., Zhang, L., Chen, D., and Wu, R.: Particle number size distributions and formation and growth rates of  
 742 different new particle formation types of a megacity in China, *J. Environ. Sci.*, 131, 11–25,  
 743 <https://doi.org/10.1016/j.jes.2022.07.029>, 2023.

- 744 [European Environment Agency \(EEA\): Air quality in Europe—2019 report.](https://www.eea.europa.eu/en/analysis/publications/air-quality-in-europe-2019)  
745 [https://www.eea.europa.eu/en/analysis/publications/air-quality-in-europe-2019, 2019.](https://www.eea.europa.eu/en/analysis/publications/air-quality-in-europe-2019)
- 746 Fuchs, N. A. and Sutugin, A. G.: HIGH-DISPERSED AEROSOLS, in: Topics in Current Aerosol Research, edited by: Hidy,  
747 G. M. and Brock, J. R., Pergamon, 1, <https://doi.org/10.1016/B978-0-08-016674-2.50006-6>, 1971.
- 748 Gordon, H., Kirkby, J., Baltensperger, U., Bianchi, F., Breitenlechner, M., Curtius, J., Dias, A., Dommen, J., Donahue, N. M.,  
749 Dunne, E. M., Duplissy, J., Ehrhart, S., Flagan, R. C., Frege, C., Fuchs, C., Hansel, A., Hoyle, C. R., Kulmala, M., Kurten, A.,  
750 Lehtipalo, K., Makhmutov, V., Molteni, U., Rissanen, M. P., Stozkhov, Y., Trostl, J., Tsagkogeorgas, G., Wagner, R.,  
751 Williamson, C., Wimmer, D., Winkler, P. M., Yan, C., and Carslaw, K. S.: Causes and importance of new particle formation  
752 in the present-day and preindustrial atmospheres, *J. Geophys. Res. Atmospheres*, 122, 8739–8760,  
753 <https://doi.org/10.1002/2017JD026844>, 2017.
- 754 Gormley, P. G. and Kennedy, M.: Diffusion from a Stream Flowing through a Cylindrical Tube, *Proc. R. Ir. Acad. Sect. Math.*  
755 *Phys. Sci.*, 52, 163–169, 1948.
- 756 Guo, S., Hu, M., Zamora, M. L., Peng, J., Shang, D., Zheng, J., Du, Z., Wu, Z., Shao, M., Zeng, L., Molina, M. J., and Zhang,  
757 R.: Elucidating severe urban haze formation in China, *Proc. Natl. Acad. Sci.*, 111, 17373–17378,  
758 <https://doi.org/10.1073/pnas.1419604111>, 2014.
- 759 Hakala, S., Vakkari, V., Bianchi, F., Dada, L., Deng, C., Dällenbach, K. R., Fu, Y., Jiang, J., Kangasluoma, J., Kujansuu, J.,  
760 Liu, Y., Petäjä, T., Wang, L., Yan, C., Kulmala, M., and Paasonen, P.: Observed coupling between air mass history, secondary  
761 growth of nucleation mode particles and aerosol pollution levels in Beijing, *Environ. Sci. Atmospheres*, 2, 146–164,  
762 <https://doi.org/10.1039/D1EA00089F>, 2022.
- 763 Hamed, A., Joutsensaari, J., Mikkonen, S., Sogacheva, L., Dal Maso, M., Kulmala, M., Cavalli, F., Fuzzi, S., Facchini, M. C.,  
764 Decesari, S., Mircea, M., Lehtinen, K. E. J., and Laaksonen, A.: Nucleation and growth of new particles in Po Valley, Italy,  
765 *Atmospheric Chem. Phys.*, 7, 355–376, <https://doi.org/10.5194/acp-7-355-2007>, 2007.
- 766 Hong, S.-Y., Dudhia, J., and Chen, S.-H.: A Revised Approach to Ice Microphysical Processes for the Bulk Parameterization  
767 of Clouds and Precipitation, 2004.
- 768 [Italian National Institute of Statistics \(ISTAT\): 2024 Annual Report - The state of a Nation.](https://www.istat.it/en/publication/2024-annual-report-the-state-of-a-nation/)  
769 [https://www.istat.it/en/publication/2024-annual-report-the-state-of-a-nation/, 2024.](https://www.istat.it/en/publication/2024-annual-report-the-state-of-a-nation/)
- 770 ~~Janjić~~Janjić, Z. I.: The Step-Mountain Eta Coordinate Model: Further Developments of the Convection, Viscous Sublayer, and  
771 Turbulence Closure Schemes, *Mon. Weather Rev.*, 122, 927–945, [https://doi.org/10.1175/1520-0493\(1994\)122%253C0927:TSMECM%253E2.0.CO;2](https://doi.org/10.1175/1520-0493(1994)122%253C0927:TSMECM%253E2.0.CO;2), 1994.
- 773 Janjić, Z. I.: A nonhydrostatic model based on a new approach, *Meteorol. Atmospheric Phys.*, 82, 271–285,  
774 <https://doi.org/10.1007/s00703-001-0587-6>, 2003.
- 775 Kerminen, V.-M., Chen, X., Vakkari, V., Petäjä, T., Kulmala, M., and Bianchi, F.: Atmospheric new particle formation and  
776 growth: review of field observations, *Environ. Res. Lett.*, 13, 103003, <https://doi.org/10.1088/1748-9326/aadf3c>, 2018.
- 777 Kontkanen, J., Järvinen, E., Manninen, H. E., Lehtipalo, K., Kangasluoma, J., Decesari, S., Gobbi, G. P., Laaksonen, A., Petäjä,  
778 T., and Kulmala, M.: High concentrations of sub-3nm clusters and frequent new particle formation observed in the Po Valley,  
779 Italy, during the PEGASOS 2012 campaign, *Atmospheric Chem. Phys.*, 16, 1919–1935, <https://doi.org/10.5194/acp-16-1919-2016>, 2016.

- 781 Kuenen, J., Dellaert, S., Visschedijk, A., Jalkanen, J.-P., Super, I., and Denier van der Gon, H.: CAMS-REG-v4: a state-of-  
782 the-art high-resolution European emission inventory for air quality modelling, *Earth Syst. Sci. Data*, 14, 491–515,  
783 <https://doi.org/10.5194/essd-14-491-2022>, 2022.
- 784 Kulmala, M., Petäjä, T., Nieminen, T., Sipilä, M., Manninen, H. E., Lehtipalo, K., Dal Maso, M., Aalto, P. P., Junninen, H.,  
785 Paasonen, P., Riipinen, I., Lehtinen, K. E. J., Laaksonen, A., and Kerminen, V.-M.: Measurement of the nucleation of  
786 atmospheric aerosol particles, *Nat. Protoc.*, 7, 1651–1667, <https://doi.org/10.1038/nprot.2012.091>, 2012.
- 787 Kulmala, M., Kontkanen, J., Junninen, H., Lehtipalo, K., Manninen, H. E., Nieminen, T., Petäjä, T., Sipilä, M., Schobesberger,  
788 S., Rantala, P., Franchin, A., Jokinen, T., Järvinen, E., Äijälä, M., Kangasluoma, J., Hakala, J., Aalto, P. P., Paasonen, P.,  
789 Mikkilä, J., Vanhanen, J., Aalto, J., Hakola, H., Makkonen, U., Ruuskanen, T., Mauldin, R. L., Duplissy, J., Vehkamäki, H.,  
790 Bäck, J., Kortelainen, A., Riipinen, I., Kurtén, T., Johnston, M. V., Smith, J. N., Ehn, M., Mentel, T. F., Lehtinen, K. E. J.,  
791 Laaksonen, A., Kerminen, V.-M., and Worsnop, D. R.: Direct observations of atmospheric aerosol nucleation, *Science*, 339,  
792 943–946, <https://doi.org/10.1126/science.1227385>, 2013.
- 793 Kulmala, M., Dada, L., Daellenbach, K. R., Yan, C., Stolzenburg, D., Kontkanen, J., Ezhova, E., Hakala, S., Tuovinen, S.,  
794 Kokkonen, T. V., Kurppa, M., Cai, R., Zhou, Y., Yin, R., Baalbaki, R., Chan, T., Chu, B., Deng, C., Fu, Y., Ge, M., He, H.,  
795 Heikkinen, L., Junninen, H., Liu, Y., Lu, Y., Nie, W., Rusanen, A., Vakkari, V., Wang, Y., Yang, G., Yao, L., Zheng, J.,  
796 Kujansuu, J., Kangasluoma, J., Petäjä, T., Paasonen, P., Järvi, L., Worsnop, D., Ding, A., Liu, Y., Wang, L., Jiang, J., Bianchi,  
797 F., and Kerminen, V.-M.: Is reducing new particle formation a plausible solution to mitigate particulate air pollution in Beijing  
798 and other Chinese megacities?, *Faraday Discuss.*, 226, 334–347, <https://doi.org/10.1039/D0FD00078G>, 2021.
- 799 Lampimäki, M., Baalbaki, R., Ahonen, L., Korhonen, F., Cai, R., Chan, T., Stolzenburg, D., Petäjä, T., Kangasluoma, J.,  
800 Vanhanen, J., and Lehtipalo, K.: Novel aerosol diluter – Size dependent characterization down to 1 nm particle size, *J. Aerosol*  
801 *Sci.*, 172, 106180, <https://doi.org/10.1016/j.jaerosci.2023.106180>, 2023.
- 802 Lehtipalo, K., Ahonen, L. R., Baalbaki, R., Sulo, J., Chan, T., Laurila, T., Dada, L., Duplissy, J., Miettinen, E., Vanhanen, J.,  
803 Kangasluoma, J., Kulmala, M., Petäjä, T., and Jokinen, T.: The standard operating procedure for Airmodus Particle Size  
804 Magnifier and nano-Condensation Nucleus Counter, *J. Aerosol Sci.*, 159, 105896,  
805 <https://doi.org/10.1016/j.jaerosci.2021.105896>, 2022.
- 806 Manninen, H. E., Mirme, S., Mirme, A., Petäjä, T., and Kulmala, M.: How to reliably detect molecular clusters and nucleation  
807 mode particles with Neutral cluster and Air Ion Spectrometer (NAIS), *Atmospheric Meas. Tech.*, 9, 3577–3605,  
808 <https://doi.org/10.5194/amt-9-3577-2016>, 2016.
- 809 ~~Maso, M. D., Kulmala, M., Riipinen, I., Wagner, R., Hussein, T., Aalto, P. P., and Lehtinen, K. E. J.: Formation and growth~~  
810 ~~of fresh atmospheric aerosols: eight years of aerosol size distribution data from SMEAR II, Hyytiälä, Finland, n.d.~~
- 811 Merikanto, J., Spracklen, D. V., Mann, G. W., Pickering, S. J., and Carslaw, K. S.: Impact of nucleation on global CCN,  
812 *Atmospheric Chem. Phys.*, 9, 8601–8616, <https://doi.org/10.5194/acp-9-8601-2009>, 2009.
- 813 [Microsoft: Bing Maps, https://www.bing.com/maps](https://www.bing.com/maps) (last access: 17 April 2025), 2025.
- 814 Mirme, S. and Mirme, A.: The mathematical principles and design of the NAIS – a spectrometer for the measurement of cluster  
815 ion and nanometer aerosol size distributions, *Atmospheric Meas. Tech.*, 6, 1061–1071, [https://doi.org/10.5194/amt-6-1061-](https://doi.org/10.5194/amt-6-1061-2013)  
816 2013, 2013.

- 817 Mlawer, E. J., Taubman, S. J., Brown, P. D., Iacono, M. J., and Clough, S. A.: Radiative transfer for inhomogeneous  
818 atmospheres: RRTM, a validated correlated-k model for the longwave, *J. Geophys. Res. Atmospheres*, 102, 16663–16682,  
819 <https://doi.org/10.1029/97JD00237>, 1997.
- 820 Nieminen, T., Kerminen, V.-M., Petäjä, T., Aalto, P. P., Arshinov, M., Asmi, E., Baltensperger, U., Beddows, D. C. S., Beukes,  
821 J. P., Collins, D., Ding, A., Harrison, R. M., Henzing, B., Hooda, R., Hu, M., Hörrak, U., Kivekäs, N., Komsaare, K., Krejci,  
822 R., Kristensson, A., Laakso, L., Laaksonen, A., Leaitch, W. R., Lihavainen, H., Mihalopoulos, N., Németh, Z., Nie, W.,  
823 O’Dowd, C., Salma, I., Sellegri, K., Svenningsson, B., Swietlicki, E., Tunved, P., Ulevicius, V., Vakkari, V., Vana, M.,  
824 Wiedensohler, A., Wu, Z., Virtanen, A., and Kulmala, M.: Global analysis of continental boundary layer new particle formation  
825 based on long-term measurements, *Atmospheric Chem. Phys.*, 18, 14737–14756, <https://doi.org/10.5194/acp-18-14737-2018>,  
826 2018.
- 827 Pushpawela, B., Jayaratne, R., and Morawska, L.: The influence of wind speed on new particle formation events in an urban  
828 environment, *Atmospheric Res.*, 215, 37–41, <https://doi.org/10.1016/j.atmosres.2018.08.023>, 2019.
- 829 Rodríguez, S., Van Dingenen, R., Putaud, J.-P., Martins-Dos Santos, S., and Roselli, D.: Nucleation and growth of new  
830 particles in the rural atmosphere of Northern Italy—relationship to air quality monitoring, *Atmos. Environ.*, 39, 6734–6746,  
831 <https://doi.org/10.1016/j.atmosenv.2005.07.036>, 2005.
- 832 Rönkkö, T., Kuuluvainen, H., Karjalainen, P., Keskinen, J., Hillamo, R., Niemi, J. V., Pirjola, L., Timonen, H. J., Saarikoski,  
833 S., Saukko, E., Järvinen, A., Silvennoinen, H., Rostedt, A., Olin, M., Yli-Ojanperä, J., Nousiainen, P., Kousa, A., and Dal  
834 Maso, M.: Traffic is a major source of atmospheric nanocluster aerosol, *Proc. Natl. Acad. Sci.*, 114, 7549–7554,  
835 <https://doi.org/10.1073/pnas.1700830114>, 2017.
- 836 Salma, I., Borsós, T., Weidinger, T., Aalto, P., Hussein, T., Dal Maso, M., and Kulmala, M.: Production, growth and properties  
837 of ultrafine atmospheric aerosol particles in an urban environment, *Atmospheric Chem. Phys.*, 11, 1339–1353,  
838 <https://doi.org/10.5194/acp-11-1339-2011>, 2011.
- 839 Savadkoobi, M., Pandolfi, M., Favez, O., Putaud, J.-P., Eleftheriadis, K., Fiebig, M., Hopke, P. K., Laj, P., Wiedensohler, A.,  
840 Alados-Arboledas, L., Bastian, S., Chazneau, B., María, Á. C., Colombi, C., Costabile, F., Green, D. C., Hueglin, C., Liakakou,  
841 E., Luoma, K., Listrani, S., Mihalopoulos, N., Marchand, N., Močnik, G., Niemi, J. V., Ondráček, J., Petit, J.-E., Rattigan, O.  
842 V., Reche, C., Timonen, H., Titos, G., Tremper, A. H., Vratolis, S., Vodička, P., Funes, E. Y., Ziková, N., Harrison, R. M.,  
843 Petäjä, T., Alastuey, A., and Querol, X.: Recommendations for reporting equivalent black carbon (eBC) mass concentrations  
844 based on long-term pan-European in-situ observations, *Environ. Int.*, 185, 108553,  
845 <https://doi.org/10.1016/j.envint.2024.108553>, 2024.
- 846 Schraufnagel, D. E.: The health effects of ultrafine particles, *Exp. Mol. Med.*, 52, 311–317, [https://doi.org/10.1038/s12276-](https://doi.org/10.1038/s12276-020-0403-3)  
847 020-0403-3, 2020.
- 848 Seinfeld, J. H. and Pandis, S. N.: *Atmospheric Chemistry and Physics: From Air Pollution to Climate Change*, John Wiley &  
849 Sons, ~~1146 pp.~~ 2016.
- 850 Simpson, D., Benedictow, A., Berge, H., Bergström, R., Emberson, L. D., Fagerli, H., Flechard, C. R., Hayman, G. D., Gauss,  
851 M., Jonson, J. E., Jenkin, M. E., Nyíri, A., Richter, C., Semeena, V. S., Tsyro, S., Tuovinen, J.-P., Valdebenito, Á., and Wind,  
852 P.: The EMEP MSC-W chemical transport model &ndash; technical description, *Atmospheric Chem. Phys.*, 12, 7825–7865,  
853 <https://doi.org/10.5194/acp-12-7825-2012>, 2012.
- 854 Spracklen, D. V., Carslaw, K. S., Kulmala, M., Kerminen, V.-M., Sihto, S.-L., Riipinen, I., Merikanto, J., Mann, G. W.,  
855 Chipperfield, M. P., Wiedensohler, A., Birmili, W., and Lihavainen, H.: Contribution of particle formation to global cloud  
856 condensation nuclei concentrations, *Geophys. Res. Lett.*, 35, <https://doi.org/10.1029/2007GL033038>, 2008.

- 857 Trechera, P., Garcia-Marlès, M., Liu, X., Reche, C., Pérez, N., Savadkoohi, M., Beddows, D., Salma, I., Vörösmarty, M.,  
858 Casans, A., Casquero-Vera, J. A., Hueglin, C., Marchand, N., Chazeau, B., Gille, G., Kalkavouras, P., Mihalopoulos, N.,  
859 Ondracek, J., Zikova, N., Niemi, J. V., Manninen, H. E., Green, D. C., Tremper, A. H., Norman, M., Vratolis, S., Eleftheriadis,  
860 K., Gómez-Moreno, F. J., Alonso-Blanco, E., Gerwig, H., Wiedensohler, A., Weinhold, K., Merkel, M., Bastian, S., Petit, J.-  
861 E., Favez, O., Crumeyrolle, S., Ferlay, N., Martins Dos Santos, S., Putaud, J.-P., Timonen, H., Lampilahti, J., Asbach, C.,  
862 Wolf, C., Kaminski, H., Altug, H., Hoffmann, B., Rich, D. Q., Pandolfi, M., Harrison, R. M., Hopke, P. K., Petäjä, T., Alastuey,  
863 A., and Querol, X.: Phenomenology of ultrafine particle concentrations and size distribution across urban Europe, *Environ.*  
864 *Int.*, 172, 107744, <https://doi.org/10.1016/j.envint.2023.107744>, 2023.
- 865 Vallabani, N. V. S., Gruzieva, O., Elihn, K., Juárez-Facio, A. T., Steimer, S. S., Kuhn, J., Silvergren, S., Portugal, J., Piña, B.,  
866 Olofsson, U., Johansson, C., and Karlsson, H. L.: Toxicity and health effects of ultrafine particles: Towards an understanding  
867 of the relative impacts of different transport modes, *Environ. Res.*, 231, 116186, <https://doi.org/10.1016/j.envres.2023.116186>,  
868 2023.
- 869 Vecchi, R., Marazzan, G., Valli, G., Ceriani, M., and Antoniazzi, C.: The role of atmospheric dispersion in the seasonal  
870 variation of PM1 and PM2.5 concentration and composition in the urban area of Milan (Italy), *Atmos. Environ.*, 38, 4437–  
871 4446, <https://doi.org/10.1016/j.atmosenv.2004.05.029>, 2004.
- 872 Wagner, R., Manninen, H. E., Franchin, A., Lehtipalo, K., Mirme, S., Steiner, G., Petäjä, T., and Kulmala, M.: On the accuracy  
873 of ion measurements using a Neutral cluster and Air Ion Spectrometer, <https://doi.org/10.1016/j.jasr.2016.03.001>, 2016.
- 874 Wang, S. C. and and Flagan, R. C.: Scanning Electrical Mobility Spectrometer, *Aerosol Sci. Technol.*, 13, 230–240,  
875 <https://doi.org/10.1080/02786829008959441>, 1990.
- 876 [Wolfram Research: Mathematica, Version 14.1, 2025.](https://www.wolfram.com/mathematica/)
- 877 [World Health Organization \(WHO\): WHO global air quality guidelines: particulate matter \(PM2.5 and PM10\), ozone, nitrogen](https://www.who.int/publications/i/item/9789240034228)  
878 [dioxide, sulfur dioxide and carbon monoxide, https://www.who.int/publications/i/item/9789240034228, 2021.](https://www.who.int/publications/i/item/9789240034228)
- 879 Yao, L., Garmash, O., Bianchi, F., Zheng, J., Yan, C., Kontkanen, J., Junninen, H., Mazon, S. B., Ehn, M., Paasonen, P., Sipilä,  
880 M., Wang, M., Wang, X., Xiao, S., Chen, H., Lu, Y., Zhang, B., Wang, D., Fu, Q., Geng, F., Li, L., Wang, H., Qiao, L., Yang,  
881 X., Chen, J., Kerminen, V.-M., Petäjä, T., Worsnop, D. R., Kulmala, M., and Wang, L.: Atmospheric new particle formation  
882 from sulfuric acid and amines in a Chinese megacity, *Science*, 361, 278–281, <https://doi.org/10.1126/science.aao4839>, 2018.
- 883 Zhao, B., Donahue, N. M., Zhang, K., Mao, L., Shrivastava, M., Ma, P.-L., Shen, J., Wang, S., Sun, J., Gordon, H., Tang, S.,  
884 Fast, J., Wang, M., Gao, Y., Yan, C., Singh, B., Li, Z., Huang, L., Lou, S., Lin, G., Wang, H., Jiang, J., Ding, A., Nie, W., Qi,  
885 X., Chi, X., and Wang, L.: Global variability in atmospheric new particle formation mechanisms, *Nature*, 631, 98–105,  
886 <https://doi.org/10.1038/s41586-024-07547-1>, 2024.
- 887 Zilitinkevich, S. and Baklanov, A.: Calculation Of The Height Of The Stable Boundary Layer In Practical Applications,  
888 *Bound.-Layer Meteorol.*, 105, 389–409, <https://doi.org/10.1023/A:1020376832738>, 2002.
- 889 Zilitinkevich, S., Esau, I., and Baklanov, A.: Further comments on the equilibrium height of neutral and stable planetary  
890 boundary layers, *Q. J. R. Meteorol. Soc.*, 133, 265–271, <https://doi.org/10.1002/qj.27>, 2007.
- 891